

Baryon-baryon scattering in a one-boson-exchange-potential approach.

II. Hyperon-nucleon scattering

M. M. Nagels, T. A. Rijken,* and J. J. de Swart

Institute for Theoretical Physics, University of Nijmegen, Nijmegen, The Netherlands

(Received 8 June 1976)

From a combined analysis of nucleon-nucleon and hyperon-nucleon scattering with a one-boson-exchange potential model the ΛN and ΣN results are presented. The model consists of local potentials due to exchanges of members of the pseudoscalar and vector-meson nonets and the scalar meson ϵ taken as a unitary singlet. The multichannel Schrödinger equation is solved in configuration space with phenomenological hard-core potentials at short distances. The coupling constants are calculated via SU(3) with the coupling constants of the NN analysis as input. Charge-symmetry breaking between the Λp and Λn channels is included. A least-squares fit to the low-energy Λp , $\Sigma^+ p$, and $\Sigma^- p$ data yields a very satisfactory result. Predictions up to the pion production threshold are given, and, whenever possible, compared to the experimental data.

I. INTRODUCTION

The hyperon-nucleon (YN) calculations of the present paper together with the nucleon-nucleon results of paper I¹ form model D in our program of constructing potential models which can describe simultaneously all experimentally studied baryon-baryon (BB) systems.

The purposes of a combined study of the NN and YN interactions are as follows:

(i) To test the assumption of SU(3) symmetry. In particular we want to investigate in this model whether a combined analysis of NN and YN is consistent with the assumption that the isosinglet scalar meson ϵ (~ 700 MeV) is dominantly a unitary singlet. Moreover, we want to determine $F/(F+D)$ ratios for the meson-baryon interaction.

(ii) To give a good theoretical description of the YN interaction by using the results for the meson-nucleon coupling constants from the NN analysis, such that in spite of the scarce experimental information many experimental quantities like scattering lengths, effective ranges, existence of resonances, etc., still can be extracted.

There is a large difference in the effort (both experimental and theoretical) which has been put in studying the NN or YN systems. The situation is now that one-boson-exchange potential (OBEP) models can give a good quantitative description of the rich and accurate NN data (for references see Ref. 2). The theoretical effort on models of YN scattering is orders of magnitude smaller than on NN scattering (for reviews see Refs. 3, 4). In addition, most of the models describe only a limited number of YN channels, for example only ΛN scattering and no ΣN scattering. Besides they usually do not show any results for NN scattering with the same model. Our model A (Ref. 5) involving OBEP from the members of the pseudoscalar- and vec-

tor-meson nonets, and the Brueckner-Watson two-pion-exchange potential gave a qualitative account of NN and a good description of YN . Models B and C (Refs. 6, 7) are pure OBEP models. These produced a reasonable quantitative fit to the NN phase shifts and showed that also the YN channels can be described well in an OBEP approach. In fact these models are the precursors of the present one. The differences are spelled out in paper I.

The meson dynamics in model D are due to the exchanges of members of the following:

(i) The pseudoscalar-meson nonet π , η , K , X^0 , with the η - X^0 mixing angle $\theta_p = -10.4^\circ$ from the Gell-Mann-Okubo mass formula.

(ii) The vector-meson nonet ρ , ϕ , K^* , ω with the ϕ - ω ideal mixing angle $\tan \theta_v = 1/\sqrt{2}$.

(iii) The scalar-meson unitary singlet ϵ . The treatment of the isosinglet meson ϵ as a unitary singlet has important consequences for YN scattering, since the coupling of the ϵ meson to all $\bar{B}B$ currents is the same in that case. In NN analyses the ω and ϵ couplings turn out to be large. The central potentials of these mesons cancel each other largely, whereas the spin-orbit forces reinforce each other to build up the strong spin-orbit potential necessary for the splitting of the 3P phase shifts in NN . When the ϵ meson is a unitary singlet, the large cancelling of the central potentials will occur in every BB channel, since the large ωNN coupling is mainly due to the large coupling of the unitary-singlet part of the ω .

Contributions of a possible octet of scalar mesons are neglected. These have all a rather high mass (~ 1.2 GeV). The reason for neglecting the scalar octet here is to prevent the introduction of one more free parameter in the YN model. In that case there would be four SU(3) parameters for the scalar nonet to be determined [the octet and sin-

glet couplings, the $F/(F+D)$ ratio, and the singlet-octet mixing angle]. In the NN analysis three coupling constants can be determined. One more free parameter in YN can then fix, in principle, the four $SU(3)$ parameters for the scalar-meson nonet. However, the scarce YN data allow only a few free parameters in order to have a nontrivial model. The effects of the contributions of an octet of scalar mesons have been studied already in model C,⁷ and will also be in the next model E.

For very short ranges ($r \lesssim 0.5$ fm) we assume a strong repulsion in all BB channels, which is described phenomenologically by using hard-core potentials.

For YN we have five free parameters, three short-range parameters, and two $F/(F+D)$ ratios. These parameters are determined in a fit to a selected set of the 35 best YN data,⁴ i.e., total cross sections for $\Lambda p \rightarrow \Lambda p$, $\Sigma^+ p \rightarrow \Sigma^+ p$, $\Sigma^- p \rightarrow \Sigma^- p$, $\Sigma^0 n$, and Λn , and r_R , the Σ^- branching ratio at rest. These experimental data are described very well by the model with $\chi^2/\text{data} = 0.65$. The same applies to the angular distributions.

The plan of the paper is as follows. In Sec. II we describe the definition of the potentials in the Lippmann-Schwinger equation. Sections III and IV give the OBEP's in momentum and configuration space. The results of the calculations for $\Sigma^+ p$, ΛN , and $\Sigma^- p$ scattering are presented and discussed in Sec. V. Section VI contains a discussion of the coupling constants and an overall discussion of the results.

II. DEFINITION OF THE POTENTIALS FOR THE LIPPMANN-SCHWINGER EQUATION

In order to have a proper prescription for how to handle field-theoretical potentials in the nonrelativistic Lippmann-Schwinger equation, we shall start with the Bethe-Salpeter equation, reducing it via the Blankenbecler-Sugar approximation into the Lippmann-Schwinger equation.

We consider the hyperon-nucleon reactions

$$Y + N \rightarrow Y' + N'. \quad (2.1)$$

In the following we often refer to Y and Y' as particles 1 and 1' (or 3) and to N and N' as particles 2 and 2' (or 4). For details of these channels see Ref. 5. The four-momentum of particle i is $p_i = (E(\vec{p}_i), \vec{p}_i)$, where $E(\vec{p}_i) = (\vec{p}_i^2 + M_i^2)^{1/2}$, and M_i is the mass. The total and relative momentum P and q are introduced by

$$p_1 = \mu_1 P + q, \quad p_2 = \mu_2 P - q, \quad (2.2)$$

with $\mu_1 + \mu_2 = 1$. Similarly we define the relative momentum q' for the particles 1' and 2'. In the

center-of-mass (c.m.) frame $P = (\sqrt{s}, \vec{0})$, $p_1 = (E_1(\vec{q}), \vec{q})$, $p_2 = (E_2(\vec{q}), -\vec{q})$, $p_{1'} = (E_{1'}(\vec{q}'), \vec{q}')$, and $p_{2'} = (E_{2'}(\vec{q}'), -\vec{q}')$, where $s = -(p_1 + p_2)^2$. Hence in the c.m. frame q and q' read

$$q = (\mu_2 E_1(\vec{q}) - \mu_1 E_2(\vec{q}), \vec{q}), \quad (2.3)$$

$$q' = (\mu_2 E_{1'}(\vec{q}') - \mu_1 E_{2'}(\vec{q}'), \vec{q}').$$

The relativistic two-particle states are normalized as (suppressing the spin dependence)

$$\langle \vec{p}'_1, \vec{p}'_2 | \vec{p}_1, \vec{p}_2 \rangle = (2\pi)^3 2E_1(\vec{p}_1) \delta^3(\vec{p}'_1 - \vec{p}_1) \times (2\pi)^3 2E_2(\vec{p}_2) \delta^3(\vec{p}'_2 - \vec{p}_2). \quad (2.4)$$

In looking for a definition of the potential for the YN channels we start with the Bethe-Salpeter equation in the c.m. frame for a transition from a state with relative four-momentum q_i to one with q_f :

$$\mathfrak{M}_{fi}(q_f, q_i; P) = \mathfrak{M}_{fi}^{\text{int}}(q_f, q_i; P) + \sum_n \int \frac{d^4 k_n}{(2\pi)^4} \mathfrak{M}_{fn}^{\text{int}}(q_f, k_n; P) G_n(k_n; P) \times \mathfrak{M}_{ni}(k_n, q_i; P). \quad (2.5)$$

\mathfrak{M}_{fi} is defined as the matrix which yields the transition-amplitude matrix M_{fi} when sandwiched between the Dirac spinors, i.e.,

$$M_{fi} = \langle f | M | i \rangle = \bar{u}_3(\vec{q}_f, s_3) \bar{u}_4(-\vec{q}_f, s_4) \mathfrak{M}_{fi}(q_f, q_i; P) \times u_1(\vec{q}_i, s_1) u_2(-\vec{q}_i, s_2). \quad (2.6)$$

The transition-amplitude matrix M_{fi} is related to the S matrix via

$$S_{fi} = \langle f | i \rangle - (2\pi)^4 i \delta^4(P_f - P_i) M_{fi}. \quad (2.7)$$

$\mathfrak{M}_{fi}^{\text{int}}(q_f, q_i; P)$ consists of the contributions of all two-particle-irreducible Feynman diagrams. The Green's function is diagonal in channel space and reads⁸

$$G_n(k_n, P) = -i \left[\frac{\gamma \cdot (\mu_1 P + k_n) + i M_{1n}}{(\mu_1 P + k_n)^2 + M_{1n}^2 - i\epsilon} \right] \times \left[\frac{\gamma \cdot (\mu_2 P - k_n) + i M_{2n}}{(\mu_2 P - k_n)^2 + M_{2n}^2 - i\epsilon} \right]. \quad (2.8)$$

The summation extends to all two-particle channels that couple to the initial and final states.

Following the procedure of Logunov and Tavkhelidze,⁹ and Blankenbecler and Sugar¹⁰ (LTBS) we write

$$G_n = g_n + (G_n - g_n), \quad (2.9)$$

and replace (2.5) by a set of two matrix equations, the LTBS equation, written in symbolic form

$$\mathfrak{M} = \mathfrak{W} + \mathfrak{W} g \mathfrak{M}, \quad (2.10)$$

and the corresponding pseudopotential equation

$$\mathfrak{W}\psi = \mathfrak{M}^{\text{irr}} + \mathfrak{M}^{\text{irr}}(G - g)\psi. \quad (2.11)$$

Two-particle unitarity is ensured when g_n is chosen to have the same singularity structure as G_n in the physical region between the two- and three-particle production threshold, i.e., when both Y_n and N_n are on the mass shell (see, e.g., Ref. 11). Hence

$\text{Im}g_n(k_n, P)$

$$\begin{aligned} &= -\frac{1}{2}[\gamma \cdot (\mu_1 P + k_n) + iM_{1n}] 2\pi i \delta^+((\mu_1 P + k_n)^2 + M_{1n}^2) \\ &\quad \times [\gamma \cdot (\mu_2 P - k_n) + iM_{2n}] 2\pi i \delta^+((\mu_2 P - k_n)^2 + M_{2n}^2) \\ &= \frac{\pi^2}{2}(-\gamma^0 E_{1n} + \vec{\gamma} \cdot \vec{k}_n + iM_{1n})(-\gamma^0 E_{2n} - \vec{\gamma} \cdot \vec{k}_n + iM_{2n}) \\ &\quad \times \delta(\sqrt{s} - E_{1n} - E_{2n}) \delta(k_n^0 - \mu_2 E_{1n} + \mu_1 E_{2n}) / (E_{1n} E_{2n}), \end{aligned} \quad (2.12)$$

where always $E_{in} = (\vec{k}_n^2 + M_{in}^2)^{1/2}$, whenever the argument has been suppressed.

Generalizing the method of Partovi and Lomon¹² to unequal-mass scattering, we rewrite the dependence on P in $\text{Im}g_n(k_n, P)$ as a function of \vec{q}_n^2 , the on-energy-shell momentum, via

$$\delta(\sqrt{s} - E_{1n} - E_{2n}) = \delta(\vec{q}_n^2 - \vec{k}_n^2) \frac{2E_{1n}E_{2n}}{E_{1n} + E_{2n}}. \quad (2.13)$$

$$\begin{aligned} \mathfrak{M}_{fi}(q_f, q_i; P) &= \mathfrak{W}_{fi}(q_f, q_i; P) + \sum_n \int \frac{d^4 k_n}{(2\pi)^4} \mathfrak{W}_{fn}(q_f, k_n; P) \frac{2M_{1n}M_{2n}}{E_{1n}(\vec{k}_n) + E_{2n}(\vec{k}_n)} \Lambda_+^{(1)}(\vec{k}_n) \\ &\quad \times \Lambda_+^{(2)}(-\vec{k}_n) \frac{2\pi \delta(k_n^0 - \mu_2 E_{1n}(\vec{q}_n) + \mu_1 E_{2n}(\vec{q}_n))}{\vec{q}_n^2 - \vec{k}_n^2 + i\epsilon} \mathfrak{M}_{ni}(k_n, q_i; P). \end{aligned} \quad (2.16)$$

So \mathfrak{M} and \mathfrak{W} can be restricted to the positive-energy states only. Using

$$2M\Lambda_+(\vec{p}) = \sum_s u(\vec{p}, s)\bar{u}(\vec{p}, s), \quad (2.17)$$

and defining the pseudopotential W analogous to (2.6)

$$W_{fi}(q_f, q_i; P) = \bar{u}_3(\vec{q}_f, s_3)\bar{u}_4(-\vec{q}_f, s_4)\mathfrak{W}_{fi}(q_f, q_i; P)u_1(\vec{q}_i, s_1)u_2(-\vec{q}_i, s_2), \quad (2.18)$$

one gets after performing the k_n^0 integration in (2.16) for the scattering matrix M_{fi}

$$M_{fi}(\vec{q}_f, \vec{q}_i; \sqrt{s}) = W_{fi}(\vec{q}_f, \vec{q}_i; \sqrt{s}) + \sum_n \int \frac{d^3 k_n}{(2\pi)^3} W_{fn}(\vec{q}_f, \vec{k}_n; \sqrt{s}) \frac{1}{2[E_{1n}(\vec{k}) + E_{2n}(\vec{k})]} \frac{1}{\vec{q}_n^2 - \vec{k}_n^2 + i\epsilon} M_{ni}(\vec{k}_n, \vec{q}_i; \sqrt{s}). \quad (2.19)$$

In (2.19) the zeroth component of k_n is given by

$$k_n^0 = \mu_2 E_{1n}(\vec{q}_n) - \mu_1 E_{2n}(\vec{q}_n). \quad (2.20)$$

Equation (2.20) can be converted into a Lippmann-Schwinger equation by introducing a nonrelativistic normalization of the two-particle states

$$(\vec{p}'_1, s'_1; \vec{p}'_2, s'_2 | \vec{p}_1, s_1; \vec{p}_2, s_2) = (2\pi)^6 \delta^3(\vec{p}'_1 - \vec{p}_1) \delta^3(\vec{p}'_2 - \vec{p}_2) \delta_{s'_1 s_1} \delta_{s'_2 s_2}, \quad (2.21)$$

and by the definition of the nonrelativistic scattering-amplitude operator T such that¹³

$$\frac{d\sigma^{fi}}{d\Omega} = \frac{|\vec{q}_f|}{|\vec{q}_i|} \left| \frac{\langle f | M | i \rangle}{8\pi\sqrt{s}} \right|^2 = \frac{|\vec{q}_f|}{|\vec{q}_i|} \left| \frac{(f | T | i)}{2\pi} \right|^2 M_{34} M_{12}, \quad (2.22)$$

We choose for $g_n(k_n, \vec{q}_n^2)$ the form

$$\begin{aligned} g_n(k_n, \vec{q}_n^2) &= -\frac{2\pi \delta(k_n^0 - \mu_2 E_{1n}(\vec{q}_n) + \mu_1 E_{2n}(\vec{q}_n))}{2(E_{1n} + E_{2n})} \\ &\quad \times \frac{1}{\vec{q}_n^2 - \vec{k}_n^2 + i\epsilon} (-\gamma^0 E_{1n} + \vec{\gamma} \cdot \vec{k}_n + iM_{1n}) \\ &\quad \times (-\gamma^0 E_{2n} - \vec{\gamma} \cdot \vec{k}_n + iM_{2n}). \end{aligned} \quad (2.14)$$

This form involving the Lippmann-Schwinger Green's function has the correct imaginary part as required by (2.12) and (2.13). The choice is far from unique (see also Ref. 11), but the occurrence of the on-shell momentum in the δ function in (2.14) has the virtue of making the potentials and thus the scattering matrix independent of the weights μ_1 and μ_2 (see the end of this section).

We note that

$$-\gamma^0 E_{1n}(\vec{k}_n) + \vec{\gamma} \cdot \vec{k}_n + iM_{1n} = 2iM_{1n} \Lambda_+^{(1)}(\vec{k}_n), \quad (2.15)$$

$$-\gamma^0 E_{2n}(\vec{k}_n) - \vec{\gamma} \cdot \vec{k}_n + iM_{2n} = 2iM_{2n} \Lambda_+^{(2)}(-\vec{k}_n),$$

where $\Lambda_+(\vec{k}_n)$ is the projection operator on positive-energy states. Therefore Eq. (2.10) can be rewritten as

where M_{34} and M_{12} are the reduced masses in the final and initial states. Another way of defining T via the nonrelativistic unitarity relation leads to the same result.¹² Generalizing the relation between M_{fi} and T_{fi} off the energy shell

$$(f|T|i) = [4M_{34}(E_3 + E_4)]^{-1/2} \langle 3, 4|M|1, 2 \rangle [4M_{12}(E_1 + E_2)]^{-1/2}, \quad (2.23)$$

yields from (2.19) the Lippmann-Schwinger equation

$$(3, 4|T|1, 2) = (3, 4|V|1, 2) + \sum_n \int \frac{d^3k_n}{(2\pi)^3} (3, 4|V|n_1, n_2) \frac{2M_{n_1 n_2}}{\bar{q}_n^2 - \bar{k}_n^2 + i\epsilon} (n_1, n_2|T|1, 2), \quad (2.24)$$

with the potential analogously to (2.23)

$$(3, 4|V|1, 2) = [4M_{34}(E_3 + E_4)]^{-1/2} \langle 3, 4|W|1, 2 \rangle [4M_{12}(E_1 + E_2)]^{-1/2}. \quad (2.25)$$

For the following it is convenient to pass to the Pauli spinor space. We define the so-called nonrelativistic amplitudes \mathcal{T} and \mathcal{V} by

$$\bar{u}_3 \bar{u}_4 T u_1 u_2 = \chi_3^\dagger \chi_4^\dagger \mathcal{T} \chi_1 \chi_2, \quad (2.26)$$

$$\bar{u}_3 \bar{u}_4 V u_1 u_2 = \chi_3^\dagger \chi_4^\dagger \mathcal{V} \chi_1 \chi_2.$$

It is easy to verify from (2.24) that the amplitude \mathcal{T} satisfies the Lippmann-Schwinger equation in 4×4 Pauli spinor space with the potential \mathcal{V}

$$(3, 4|\mathcal{T}|1, 2) = (3, 4|\mathcal{V}|1, 2) + \sum_n \int \frac{d^3k_n}{(2\pi)^3} (3, 4|\mathcal{V}|n_1, n_2) \frac{2M_{n_1 n_2}}{\bar{q}_n^2 - \bar{k}_n^2 + i\epsilon} (n_1, n_2|\mathcal{T}|1, 2). \quad (2.27)$$

Using rotational invariance and parity conservation one can expand the 4×4 transition matrix \mathcal{T} (Refs. 14, 4)

$$\mathcal{T} = \sum_{i=1}^8 \mathcal{T}_i P_i, \quad (2.28)$$

where $\mathcal{T}_i = \mathcal{T}_i(\bar{q}_f^2, \bar{q}_i^2, \bar{q}_i \cdot \bar{q}_f)$. We shall choose for the operators P_i in spin-space⁴

$$\begin{aligned} P_1 &= 1, & P_2 &= \bar{\sigma}_1 \cdot \bar{\sigma}_2, \\ P_3 &= (\bar{\sigma}_1 \cdot \bar{k})(\bar{\sigma}_2 \cdot \bar{k}), & P_4 &= (i/2)(\bar{\sigma}_1 + \bar{\sigma}_2) \cdot \bar{n}, \\ P_5 &= (\bar{\sigma}_1 \cdot \bar{n})(\bar{\sigma}_2 \cdot \bar{n}), & P_6 &= (i/2)(\bar{\sigma}_1 - \bar{\sigma}_2) \cdot \bar{n}, \\ P_7 &= (\bar{\sigma}_1 \cdot \bar{q})(\bar{\sigma}_2 \cdot \bar{k}) + (\bar{\sigma}_1 \cdot \bar{k})(\bar{\sigma}_2 \cdot \bar{q}), \\ P_8 &= (\bar{\sigma}_1 \cdot \bar{q})(\bar{\sigma}_2 \cdot \bar{k}) - (\bar{\sigma}_1 \cdot \bar{k})(\bar{\sigma}_2 \cdot \bar{q}), \end{aligned} \quad (2.29)$$

where

$$\begin{aligned} \bar{q} &= (\bar{q}_i + \bar{q}_f)/2, \\ \bar{k} &= \bar{q}_f - \bar{q}_i, \\ \bar{n} &= \bar{q}_i \times \bar{q}_f = \bar{k} \times \bar{q}. \end{aligned} \quad (2.30)$$

A similar expansion can be made for the potential \mathcal{V} .

Finally, we consider the dependence of the potentials on the weights μ_1 and μ_2 . The zeroth components of the momenta occur only in the combination $p_1^0 - p_{1n}^0$, e.g., in the propagators for meson exchanges $[(p_1 - p_{1n})^2 + m^2]^{-1}$. With our choice of $g_n(k_n, P)$, Eq. (2.14), we have in the potentials

$$\begin{aligned} p_1^0 - p_{1n}^0 &= \mu_2 E_1(\bar{q}) - \mu_1 E_2(\bar{q}) - \mu_2 E_{1n}(\bar{q}_n) + \mu_1 E_{2n}(\bar{q}_n) \\ &= E_1(\bar{q}) - E_{1n}(\bar{q}_n), \end{aligned} \quad (2.31)$$

and therefore

$$\begin{aligned} \mathcal{V}(\bar{q}, \bar{k}_n, \sqrt{s}) &\sim \{ -[E_1(\bar{q}) - E_{1n}(\bar{q}_n)]^2 \\ &\quad + (\bar{q} - \bar{k}_n)^2 + m^2 \}^{-1}, \end{aligned} \quad (2.32)$$

i.e., independent of the weights μ_1 and μ_2 .

In the case of nonzero contributions of $[E_1(\bar{q}) - E_{1n}(\bar{q}_n)]^2$ (e.g., $\Lambda\Sigma$ transitions or strange-meson exchanges) we approximate

$$(p_1 - p_{1n})^2 + m^2 \simeq (\bar{p}_1 - \bar{p}_{1n})^2 + \bar{m}^2 \quad (2.33)$$

by absorbing $(E_1 - E_{1n})^2$ into the mass term by changing the mass to an effective mass \bar{m} . All cases of interest to us are discussed extensively in Ref. 4.

III. OBEP IN MOMENTUM SPACE

In the OBEP approximation we consider only second-order irreducible diagrams contributing to the kernel

$$W = M^{1rr(2)}. \quad (3.1)$$

Similarly to (2.28) we expand the nonrelativistic potentials \mathcal{V} as

$$\mathcal{V} = \sum_{i=1}^8 \mathcal{V}_i P_i, \quad (3.2)$$

where the P_i are given in (2.29). This means that

we neglect the potential forms P_7 and P_8 . In this paper we will make the local approximation for \mathcal{V}_i . Terms like P_7 and P_8 would lead to nonlocal potentials and hence are neglected. In deriving these local functions $\mathcal{V}_i(\vec{k}^2)$ we make the following approximations:

$$(i) E = (\vec{k}^2/4 + \vec{q}^2 + M^2)^{1/2} \simeq M + \vec{k}^2/8M. \quad (3.3)$$

$$(ii) 1/M_N^2 + 1/M_Y^2 \simeq 2/(M_N M_Y). \quad (3.4)$$

(iii) We keep only terms up to order \vec{k}^2/M^2 .

(iv) In the meson propagators $[(p_1 - p_3)^2 + m^2] \simeq (\vec{k}^2 + \bar{m}^2)$ [cf. (2.33)]. When two different hyperons are involved ($\Lambda\Sigma$) the average mass is used in the potentials.

The interaction Hamiltonian densities are

(i) pseudoscalar-meson exchange

$$\mathcal{H}_P = ig_{13} \bar{\psi}_3 \gamma_5 \psi_1 \phi, \quad (3.5)$$

(ii) scalar-meson exchange

$$\mathcal{H}_S = g_{13} \bar{\psi}_3 \psi_1 \phi, \quad (3.6)$$

(iii) vector-meson exchange

$$\mathcal{H}_V = ig_{13} \bar{\psi}_3 \gamma_\mu \psi_1 \phi^\mu + \frac{f_{13}}{4\mathfrak{N}} \bar{\psi}_3 \sigma_{\mu\nu} \psi_1 (\partial^\mu \phi^\nu - \partial^\nu \phi^\mu). \quad (3.7)$$

Similar interactions apply to the 24 vertex. The scaling mass \mathfrak{M} in (3.7) is chosen to be the proton mass.

Using the approximations described above we find, for the \mathcal{V}_i in the case of nonstrange-meson exchange,

(i) pseudoscalar-meson exchange

$$\mathcal{V}_3^P = -g_{13} g_{24} \Delta / (4M_Y M_N), \quad (3.8)$$

(ii) scalar-meson exchange

$$\begin{aligned} \mathcal{V}_1^S &= -g_{13} g_{24} [1 + \vec{k}^2 / (8M_Y M_N)] \Delta, \\ \mathcal{V}_4^S &= g_{13} g_{24} \Delta / (2M_Y M_N), \\ \mathcal{V}_5^S &= g_{13} g_{24} \Delta / (16M_Y^2 M_N^2), \\ \mathcal{V}_6^S &= g_{13} g_{24} \Delta (M_Y^2 - M_N^2) / (4M_Y^2 M_N^2), \end{aligned} \quad (3.9)$$

IV. THE POTENTIAL MODEL IN CONFIGURATION SPACE

The potentials in configuration space are obtained via Fourier transformation.¹⁶ The additional approximation of the quadratic spin-orbit terms is described in paper I.¹ From (3.8)–(3.10) we get

(i) pseudoscalar-meson exchange

$$V^P(r) = \frac{g_{13} g_{24}}{4\pi} \frac{m^2}{4M_Y M_N} m \left[\frac{1}{3} (\vec{\sigma}_1 \cdot \vec{\sigma}_2) \phi(x) + S_{12} \chi(x) \right] \mathcal{O}, \quad (4.1)$$

(ii) scalar-meson exchange

$$\begin{aligned} V^S(r) = & -\frac{g_{13} g_{24}}{4\pi} m \left[\left(1 - \frac{m^2}{8M_Y M_N} \right) \phi(x) + \frac{m^2}{2M_Y M_N} \left(\frac{1}{x} + \frac{1}{x^2} \right) \phi(x) \vec{L} \cdot \vec{S} + \frac{m^4}{16M_Y^2 M_N^2} \frac{3}{x^2} \chi(x) Q_{12} \right. \\ & \left. + \frac{m^2 (M_Y^2 - M_N^2)}{4M_Y^2 M_N^2} \left(\frac{1}{x} + \frac{1}{x^2} \right) \phi(x) \frac{1}{2} (\vec{\sigma}_1 - \vec{\sigma}_2) \cdot \vec{L} \right] \mathcal{O}, \end{aligned} \quad (4.2)$$

(iii) vector-meson exchange

$$\mathcal{V}_1^V = \{ g_{13} g_{24} [1 - \vec{k}^2 / (8M_Y M_N)] - g_{13} f_{24} \vec{k}^2 / (4\mathfrak{N} M_N) - g_{24} f_{13} \vec{k}^2 / (4\mathfrak{N} M_Y) + f_{13} f_{24} \vec{k}^4 / (16\mathfrak{N}^2 M_Y M_N) \} \Delta,$$

$$\mathcal{V}_2^V = -\vec{k}^2 \mathcal{V}_3^V,$$

$$\mathcal{V}_3^V = \{ g_{13} g_{24} + g_{13} f_{24} M_N / \mathfrak{N} + g_{24} f_{13} M_Y / \mathfrak{N} + f_{13} f_{24} [1 - \vec{k}^2 / (8M_Y M_N)] M_Y M_N / \mathfrak{N}^2 \} \Delta / (4M_Y M_N),$$

$$\mathcal{V}_4^V = [12g_{13} g_{24} + 8(g_{13} f_{24} + g_{24} f_{13}) (M_Y M_N)^{1/2} / \mathfrak{N} - f_{13} f_{24} 3\vec{k}^2 / \mathfrak{N}^2] \Delta / (8M_Y M_N),$$

$$\mathcal{V}_5^V = -[g_{13} g_{24} + (g_{13} f_{24} + g_{24} f_{13}) 4(M_Y M_N)^{1/2} / \mathfrak{N} + f_{13} f_{24} 8M_Y M_N / \mathfrak{N}^2] \Delta / (16M_Y^2 M_N^2),$$

$$\mathcal{V}_6^V = [(g_{13} g_{24} + f_{13} f_{24} \vec{k}^2 / 4\mathfrak{N}^2) (M_Y^2 - M_N^2) / (4M_Y^2 M_N^2) - (g_{13} f_{24} - g_{24} f_{13}) / (\mathfrak{N} M_Y^{1/2} M_N^{1/2})] \Delta, \quad (3.10)$$

where

$$\Delta = (\vec{k}^2 + \bar{m}^2)^{-1}. \quad (3.11)$$

For the mesons carrying hypercharge (K and K^*) we find a completely symmetrical occurrence of M_Y and M_N and an additional minus sign.¹⁵ The potentials can be obtained from (3.8)–(3.10) by replacing both M_Y and M_N by $(M_Y M_N)^{1/2}$ and adding a minus sign. Furthermore we get nonzero contributions from the second part of the vector-meson propagator ($k^\mu k^\nu / m^2$). Hence we have¹⁵

$$-\mathcal{V}^{K^*} = \mathcal{V}^V - (M_3 - M_1)(M_4 - M_2) \mathcal{V}^{(S)} / m^2, \quad (3.12)$$

where in $\mathcal{V}^{(S)}$ the vector-meson coupling constants $g_{13} g_{24}$ have to be inserted, and M_Y and M_N have to be replaced by $(M_Y M_N)^{1/2}$.

(iii) vector-meson exchange

$$\begin{aligned}
V^V(r) = & \frac{m}{4\pi} \left\{ \left[g_{13}g_{24} \left(1 + \frac{m^2}{8M_Y M_N} \right) + g_{13}f_{24} \frac{m^2}{4\mathfrak{M}M_N} + g_{24}f_{13} \frac{m^2}{4\mathfrak{M}M_Y} + f_{13}f_{24} \frac{m^4}{16\mathfrak{M}^2 M_Y M_N} \right] \phi(x) \right. \\
& - \frac{m^2}{M_Y M_N} \left[\frac{3}{2} g_{13}g_{24} + (g_{13}f_{24} + g_{24}f_{13}) \frac{(M_Y M_N)^{1/2}}{\mathfrak{M}} + f_{13}f_{24} \frac{3m^2}{8\mathfrak{M}^2} \right] \left(\frac{1}{x} + \frac{1}{x^2} \right) \phi(x) \vec{L} \cdot \vec{S} \\
& + \frac{m^2}{4M_Y M_N} \left[g_{13}g_{24} + g_{13}f_{24} \frac{M_N}{\mathfrak{M}} + g_{24}f_{13} \frac{M_Y}{\mathfrak{M}} + f_{13}f_{24} \frac{M_Y M_N}{\mathfrak{M}^2} \left(1 + \frac{m^2}{8M_Y M_N} \right) \right] \left[\frac{2}{3} (\vec{\sigma}_1 \cdot \vec{\sigma}_2) \phi(x) - S_{12} \chi(x) \right] \\
& + \frac{m^4}{16M_Y^2 M_N^2} \left[g_{13}g_{24} + (g_{13}f_{24} + g_{24}f_{13}) \frac{4(M_Y M_N)^{1/2}}{\mathfrak{M}} + f_{13}f_{24} \frac{8M_Y M_N}{\mathfrak{M}^2} \right] \frac{3}{x^2} \chi(x) Q_{12} \\
& - \left. \left[\left(g_{13}g_{24} - f_{13}f_{24} \frac{m^2}{4\mathfrak{M}^2} \right) \frac{m^2(M_Y^2 - M_N^2)}{4M_Y^2 M_N^2} - (g_{13}f_{24} - g_{24}f_{13}) \frac{m^2}{\mathfrak{M}(M_Y M_N)^{1/2}} \right] \left(\frac{1}{x} + \frac{1}{x^2} \right) \phi(x) \frac{1}{2} (\vec{\sigma}_1 - \vec{\sigma}_2) \cdot \vec{L} \right\} \phi.
\end{aligned} \tag{4.3}$$

In these formulas $x = mr$, where m is the average mass of the isomultiplet, and

$$\phi(x) = e^{-x}/x, \quad \chi(x) = \left(\frac{1}{3} + 1/x + 1/x^2 \right) e^{-x}/x, \tag{4.4}$$

$$Q_{12} = \frac{1}{2} [(\vec{\sigma}_1 \cdot \vec{L})(\vec{\sigma}_2 \cdot \vec{L}) + (\vec{\sigma}_2 \cdot \vec{L})(\vec{\sigma}_1 \cdot \vec{L})]. \tag{4.5}$$

$\mathcal{P} = 1$ for hypercharge $Y = 0$ exchanges and

$$\mathcal{P} = -\mathcal{P}_x \mathcal{P}_\sigma \tag{4.6}$$

for $Y \neq 0$ exchanges (K, K^*), where \mathcal{P}_x and \mathcal{P}_σ denote the space and spin exchange operators. In the latter case we have to replace both M_Y and M_N by $(M_Y M_N)^{1/2}$ in the expressions (4.1)–(4.3) and reverse the sign of the antisymmetric spin-orbit term $\frac{1}{2}(\vec{\sigma}_1 - \vec{\sigma}_2) \cdot \vec{L}$.¹⁵ For K^* exchange we have in addition to (4.11) also the term

$$V^{K^*} = - \frac{(M_3 - M_1)(M_4 - M_2)}{m^2} V^S, \tag{4.7}$$

where in V^S the vector-meson couplings $g_{13}g_{24}$ have to be inserted.

Our treatment of the relevant baryon-baryon channels and their SU(3) classification has been described in detail in Ref. 5. There also the SU(3) conventions for the coupling constants are spelled out. We mention two differences. Firstly, we do not use here any SU(6) relation for the coupling constants, although we keep $\alpha_V^0 = 1$ for the direct coupling of the vector mesons, thus coupling the ρ meson universally to the isospin current. The NN coupling constants having been determined in paper I, we determine in this YN analysis α_P and α_V^m . Secondly we have included $\eta - X^0$ mixing

$$\begin{aligned}
|X^0\rangle &= \cos\theta_P |X_1^0\rangle + \sin\theta_P |\eta_8\rangle, \\
|\eta\rangle &= -\sin\theta_P |X_1^0\rangle + \cos\theta_P |\eta_8\rangle,
\end{aligned} \tag{4.8}$$

The singlet-octet mixing angle is taken from the Gell-Mann–Okubo mass formula $\theta_P = -10.4^\circ$. The treatment of the broad mesons ρ and ϵ has been

described extensively in paper I.

The hard-core scheme for the s waves in YN reads (for more extensive discussion see Refs. 1 and 5)

$$\begin{aligned}
x_s & \text{ hard core in } {}^1S_0(\Lambda N; \Sigma N, I = \frac{1}{2}, \frac{3}{2}), \\
\lambda & \text{ modification parameter in } {}^1S_0(\Sigma N, I = \frac{3}{2}), \\
x_t & \text{ hard core in } {}^3S_1 - {}^3D_1(\Lambda N; \Sigma N, I = \frac{1}{2}, \frac{3}{2}).
\end{aligned} \tag{4.9}$$

In order to be able to calculate in the particle basis, we account for the difference which can exist in principle between the hard cores of $\Sigma N(I = \frac{1}{2})$ and $\Sigma N(I = \frac{3}{2})$ in the 1S_0 wave by multiplying the potentials in the $I = \frac{3}{2}$ state by a phenomenological function

$$\xi(r) = 1 - \exp[-(r-x)/\lambda]. \tag{4.10}$$

The modification parameter λ is required to be small such that only the inner part of the potentials is affected, and the tail is still determined by meson exchanges only.

The treatment of the hard cores in the p and higher L waves is discussed in Sec. V A.

V. RESULTS OF THE CALCULATIONS

A. Determining of the free parameters

Having obtained in the NN analysis¹ the values for the coupling constants of the nonstrange mesons with the nucleons, all meson-baryon coupling constants can be calculated via SU(3) relations. But we still need to determine the short-range parameters and the $F/(F+D)$ ratio of the pseudoscalar-meson octet. Furthermore, we check the value of α_V^m keeping $f_{\omega NN}$ fixed in view of the small sensitivity of NN to $f_{\phi NN}$.¹

Tracing the dependence of the s waves on the hard-core radii, we find that the ${}^3S_1(\Sigma N, I = \frac{3}{2})$ potential is always weak and repulsive. Therefore the dependence of the ${}^3S_1(\Sigma N, I = \frac{3}{2})$ scattering

length and the total nuclear cross section on the hard-core radius is very weak.¹⁵ So we can take the hard-core radius $x_p(\Sigma N, I=\frac{3}{2})$ the same as $x_t(\Lambda N; \Sigma N, I=\frac{1}{2}) \equiv x_t$.

For the p waves in NN we found that a single hard-core $x_p=0.34594$ fm was sufficient for the potentials in both the $I=1$ and $I=0$ states. The $^1P_1(NN)$ potential, which is in the 10^* , is repulsive and hence insensitive to hard-core variations. In the $^3P(NN)$ waves, which belong to the 27 , the $^3P_1(NN)$ potential and the inner part of the $^3P_0(NN)$ potential are repulsive, but the $^3P_2(NN)$ potential is attractive at short distances. So x_p in NN is essentially determined by the 3P_2 phase shifts. Considering the p waves in YN , we notice that in the 1P_1 waves apart from the potentials in the 10^* also potentials in the 10 and 8_a occur, and in the 3P waves next to potentials in the 27 also potentials occur in the 8_s representation. We have performed a tedious investigation of the hard-core dependence of the various p waves in YN with the following results¹⁵:

- (i) For $\Sigma N, I=\frac{3}{2}$ we have
 - (a) strong dependence of 1P_1 , leading to $x > 0.40$ fm,
 - (b) almost no dependence of 3P_0 ,
 - (c) almost no dependence of 3P_1 ,
 - (d) slight dependence of 3P_2 - 3F_2 .
- (ii) For ΛN and $\Sigma N, I=\frac{1}{2}$ we have
 - (a) strong dependence of 1P_1 , leading to $x > 0.39$ fm,
 - (b) almost no dependence of 3P_0 ,
 - (c) moderate dependence of 3P_1 ,
 - (d) strong dependence of 3P_2 - 3F_2 , leading to $x > 0.34$ fm.

We try to describe the p waves in YN with a single hard-core radius $x_p > 0.40$ fm. The value of x_p can be searched by fitting to the data that depend genuinely on the p waves: the angular distributions of $\Sigma^*p \rightarrow \Sigma^*p$ at $p_{\Sigma^*} = 170$ MeV/c and of $\Sigma^*p \rightarrow \Sigma^*p$ and $\Sigma^*p \rightarrow \Lambda n$ at $p_{\Sigma^*} = 160$ MeV/c. The results show that indeed with a single hard-core radius for the p waves we can get an excellent description of the experimental angular distributions. It appears that the best fits are obtained when $x_p \approx 0.31 m_\pi^{-1}$. Hence we have kept

$$x_p = 0.31 m_\pi^{-1} = 0.44314 \text{ fm}, \quad (5.1)$$

leading to $\chi^2 = 2.9$ for seven Σ^*p differential-cross-section data and $\chi^2 = 12.4$ for the six $\Sigma^*p \rightarrow \Sigma^*p$ together with ten $\Sigma^*p \rightarrow \Lambda n$ differential-cross-section data.

For the higher L waves ($L \geq 2$) we have no clue to determine the hard-core radius $x_{L \geq 2}$ in YN . In view of the small sensitivity of these peripheral waves to hard-core variations, we just take over in YN the hard-core radius needed in NN (Ref. 1)

$$x_{L \geq 2} = 0.66254 \text{ fm}. \quad (5.2)$$

The last step is the determination of the five free parameters: three s -wave short-range parameters (x_s, λ, x_t), α_P , and α_V^m (thereby keeping $f_{NN\rho}$ and $f_{NN\omega}$ fixed). This is done in a least-squares fit to the selected set of the best 35 YN data [Table I (data are from Refs. 17-19, 26, 27)]. The values which emerge are given in Table II together with the covariance matrix α^{-1} and the correlation matrix C . In Table I we compare our calculated values with the experimental ones. The total $\chi^2 = 19.5$ for 35 data and 5 degrees of freedom, i.e., $\chi^2/\text{data} = 0.65$.

We shall present the results concisely. Those who need more details can get these on request.

B. Σ^*p scattering

The values of the five free parameters from the overall fit lead to the scattering lengths and effective ranges of the Σ^*p s waves with statistical

TABLE I. Comparison of the theoretical and experimental values for the selected set of 35 best YN data (Ref. 5). The superscripts RH and M indicate the Rehovoth-Heidelberg (Ref. 17) and Maryland (Ref. 18) Λp data. The lab momenta are given in MeV/c and the cross sections in mb.

$\Lambda p \rightarrow \Lambda p \quad \chi^2 = 3.1$			$\Lambda p \rightarrow \Lambda p \quad \chi^2 = 1.9$		
p_Λ	$\sigma_{\text{exp}}^{\text{RH}}$	σ_{th}	p_Λ	$\sigma_{\text{exp}}^{\text{M}}$	σ_{th}
145	180 ± 22	210.2	135	209 ± 58	229.9
185	130 ± 17	145.6	165	177 ± 38	175.2
210	118 ± 16	115.4	195	153 ± 27	132.7
230	101 ± 12	95.9	225	111 ± 18	100.4
250	83 ± 9	79.7	255	87 ± 13	76.1
290	57 ± 9	55.4	300	46 ± 11	50.7
$\Sigma^*p \rightarrow \Sigma^*p \quad \chi^2 = 0.1$			$\Sigma^*p \rightarrow \Sigma^*p \quad \chi^2 = 3.6$		
p_{Σ^*}	σ_{exp}	σ_{th}	p_{Σ^*}	σ_{exp}	σ_{th}
145	123 ± 62	108.5	142.5	152 ± 38	142.0
155	104 ± 30	99.1	147.5	146 ± 30	134.6
165	92 ± 18	91.1	152.5	142 ± 25	128.1
175	81 ± 12	83.7	157.5	164 ± 32	122.1
			162.5	138 ± 19	116.3
			167.5	113 ± 16	111.2
$\Sigma^*p \rightarrow \Sigma^0 n \quad \chi^2 = 5.5$			$\Sigma^*p \rightarrow \Lambda n \quad \chi^2 = 4.3$		
p_{Σ^*}	σ_{exp}	σ_{th}	p_{Σ^*}	σ_{exp}	σ_{th}
110	396 ± 91	192.9	110	174 ± 47	236.3
120	159 ± 43	168.4	120	178 ± 39	201.4
130	157 ± 34	149.0	130	140 ± 28	174.1
140	125 ± 25	133.4	140	164 ± 25	152.3
150	111 ± 19	120.6	150	147 ± 19	134.7
160	115 ± 16	110.2	160	124 ± 14	120.3
$r_R^{\text{exp}} = 0.468 \pm 0.010$			$r_R^{\text{th}} = 0.4775 \quad \chi^2 = 0.9$		

errors

$$a_s^C = -3.66 \pm 0.33 \text{ fm}, \quad r_s^C = 3.52 \pm 0.25 \text{ fm}, \quad (5.3)$$

$$a_t^C = 0.34 \pm 0.01 \text{ fm}, \quad r_t^C = -7.31 \pm 0.20 \text{ fm},$$

where the superscript C denotes the presence of the Coulomb potential.

For the case that the Coulomb interaction is not present as in $\Sigma^- n$ scattering we obtain

$$a_s = -4.61 \pm 0.60 \text{ fm}, \quad r_s = 3.69 \pm 0.27 \text{ fm}, \quad (5.4)$$

$$a_t = 0.32 \pm 0.01 \text{ fm}, \quad r_t = -6.01 \pm 0.12 \text{ fm}.$$

The $\Sigma^+ p$ "total" cross sections (for definition see Ref. 5) are compared with the experimental values in Table I and Fig. 1. An excellent fit is obtained, since we have here essentially one free parameter (λ), which fixes the ${}^1S_0 (I = \frac{3}{2})$ contribution.

In Fig. 2 we compare the calculated values with the experimental angular distribution from the Heidelberg group,¹⁹ showing good agreement. A few remarks can be made about the differential cross sections. The Coulomb interference with the triplet waves, which is almost entirely due to the 3S_1 wave, is constructive. The destructive Coulomb interference with the singlet waves, which is almost completely due to the 1S_0 wave, is larger in absolute value yielding a total destructive Coulomb-interference result. The shape of the angular distribution, however, is apart from the Coulomb forward peak essentially determined by the 1S_0 - 1P_1 interference term, which is large.

We have calculated also the polarization of the scattered Σ^+ along the normal at $p_{\Sigma^+} = 170 \text{ MeV}/c$. The result is $\langle \vec{P} \cdot \hat{n} \rangle = -0.001$, and it agrees with

TABLE II. Values of the free parameters in the best-fit point and the covariance matrix α^{-1} in units of fm together with the correlation matrix C .

x_s (fm)	x_t (fm)	λ (fm)	α_P	$\alpha_{\vec{P}}$
0.562 71	0.449 15	0.075 45	0.464 03	0.334 28

$$\alpha^{-1} = \begin{bmatrix} 0.49 & -0.16 & -1.55 & -0.02 & -0.00 \\ -0.16 & 0.11 & 0.49 & -0.01 & 0.01 \\ -1.55 & 0.49 & 9.35 & 0.46 & 0.00 \\ -0.02 & -0.01 & 0.46 & 0.58 & -0.02 \\ -0.00 & 0.01 & 0.00 & -0.02 & 0.05 \end{bmatrix} \times 10^{-4}$$

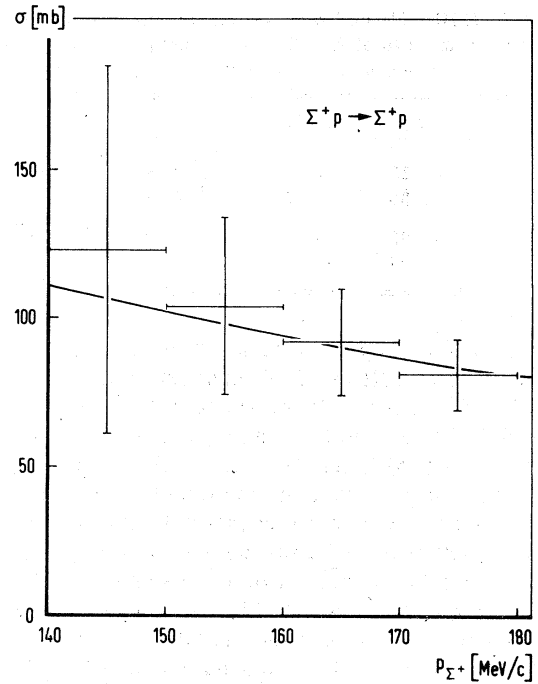
$$C = \begin{bmatrix} 1 & -0.71 & -0.73 & -0.04 & -0.03 \\ -0.71 & 1 & 0.50 & -0.06 & 0.14 \\ -0.73 & 0.50 & 1 & 0.20 & 0.01 \\ -0.04 & -0.06 & 0.20 & 1 & -0.10 \\ -0.03 & 0.14 & 0.01 & -0.10 & 1 \end{bmatrix}$$


FIG. 1. Calculated $\Sigma^+ p$ "total" cross sections compared with experimental values of Ref. 19.

the measured value¹⁹ $\langle \vec{P} \cdot \hat{n} \rangle = 0.0 \pm 0.16$. Note that no singlet waves contribute to this polarization,¹⁵ which are the only ones with slightly larger phase shifts.

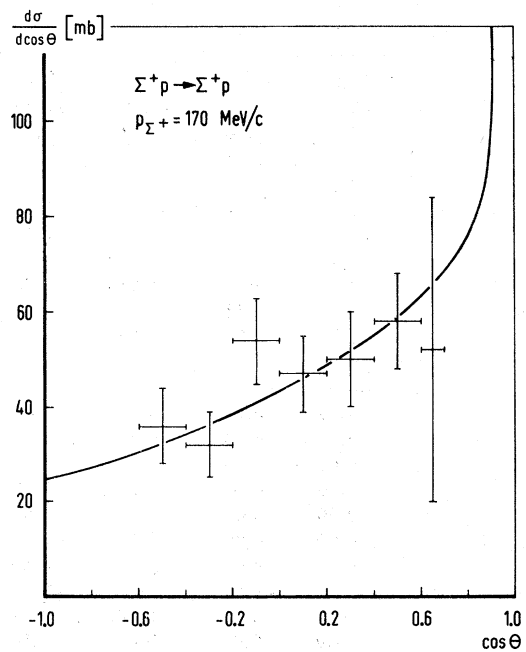


FIG. 2. Calculated $\Sigma^+ p$ differential cross sections compared with the data of Ref. 19.

TABLE III. Σ^*p and Σ^*n p -wave effective-range parameters in units of fm. The superscript C denotes the presence of the Coulomb interaction.

	1P_1	3P_0	3P_1	3P_2
a^C	-2.13	-2.46	1.49	-0.244
r^C	2.39	4.29	-9.18	6.75
a	-1.82	-2.01	1.20	-0.214
r	2.24	4.91	-11.20	13.50

The p -wave Σ^*p low-energy parameters are given in Table III for the expansions Eqs. (30) and (32) of paper I. When we compare the values of the $^3P(\Sigma^*p)$ effective-range parameters with those of $^3P(pp)$ (Table V of paper I), we see that the sign and the order of magnitude is the same, as we expect from the fact that both $^3P(pp)$ and $^3P(\Sigma^*p)$ are in the 27 representation of SU(3).

In Table IV the nuclear-bar phase shifts for Σ^*p are given as predicted by the model. In particular we want to mention the 1P_1 phase shifts, which grow to about 75° around $p_{\Sigma^*} = 660$ MeV/c. In Fig. 3 we have depicted the total nuclear cross section of Σ^*p . Very interesting is the maximum around $p_{\Sigma^*} = 420$ MeV/c, which is essentially due to the large 1P_1 phase shift.

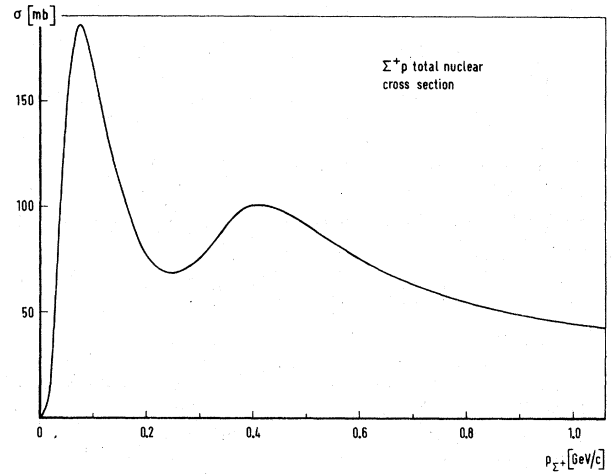


FIG. 3. Σ^*p total nuclear cross sections as predicted by the model.

C. ΛN scattering

In our ΛN calculations we get different values for the low-energy parameters in the charge +1 and 0 states, since we have taken into account charge-symmetry-breaking potentials. The s -wave scattering lengths and effective ranges are given in Table V for Λp , Λn , and for ΛN , suppressing the

TABLE IV. Σ^*p nuclear-bar phase shifts in degrees. The ρ_i denote the mixing angles for $^1J_J \leftrightarrow ^3J_J$.

p_{Σ^*} (MeV/c)	100	200	300	400	500	600	700	800	900	1000
T_{lab} (MeV)	4.2	16.7	37.2	65.5	100.8	142.8	190.7	244.0	302.1	364.5
1S_0	30.36	36.83	31.58	23.47	14.60	5.66	-3.08	-11.51	-19.59	-27.34
3S_1	-3.06	-6.92	-11.57	-17.20	-23.48	-30.01	-36.52	-42.84	-48.91	-54.71
ϵ_1	-0.38	-1.86	-3.42	-4.53	-5.14	-5.32	-5.20	-4.88	-4.44	-3.95
3P_0	0.94	4.95	8.80	9.89	8.14	4.39	-0.55	-6.12	-12.00	-17.95
1P_1	0.94	7.75	26.18	52.25	68.74	74.55	74.57	71.46	68.16	64.78
ρ_1	-0.00	-0.02	-0.08	-0.16	-0.20	-0.21	-0.22	-0.23	-0.23	-0.24
3P_1	-0.53	-2.62	-5.09	-7.49	-9.92	-12.54	-15.05	-17.15	-20.45	-24.36
3P_2	0.12	1.10	3.21	5.83	8.05	9.32	9.52	8.82	7.44	5.59
ϵ_2	-0.03	-0.35	-1.01	-1.72	-2.28	-2.58	-2.65	-2.51	-2.23	-1.85
3D_1	0.02	0.29	0.89	1.60	2.16	2.29	1.83	0.70	-1.04	-3.30
1D_2	0.02	0.30	0.96	2.05	3.68	5.79	8.16	10.46	12.36	13.63
ρ_2	-0.00	-0.00	-0.00	-0.01	-0.02	-0.03	-0.05	-0.06	-0.07	-0.08
3D_2	-0.03	-0.42	-1.21	-2.11	-2.95	-3.75	-4.60	-5.60	-6.80	-8.24
3D_3	0.00	0.06	0.33	0.94	1.92	3.12	4.30	5.23	5.75	5.77
ϵ_3	-0.00	-0.06	-0.28	-0.61	-1.00	-1.37	-1.69	-1.93	-2.10	-2.18
3F_2	0.00	0.03	0.16	0.40	0.70	1.03	1.31	1.45	1.37	1.02
1F_3	0.00	0.05	0.22	0.49	0.88	1.43	2.17	3.15	4.33	5.67
ρ_3	-0.00	-0.00	-0.00	-0.00	-0.00	-0.01	-0.01	-0.02	-0.03	-0.04
3F_3	-0.00	-0.08	-0.34	-0.75	-1.20	-1.62	-1.97	-2.26	-2.51	-2.77
3F_4	0.00	0.01	0.04	0.16	0.40	0.81	1.39	2.13	2.98	3.87
ϵ_4	-0.00	-0.01	-0.08	-0.23	-0.43	-0.65	-0.88	-1.10	-1.29	-1.46
3G_3	0.00	0.01	0.04	0.11	0.24	0.40	0.59	0.79	0.96	1.09
1G_4	0.00	0.01	0.07	0.18	0.33	0.52	0.76	1.07	1.48	2.00
3G_4	-0.00	-0.01	-0.10	-0.28	-0.53	-0.80	-1.06	-1.29	-1.47	-1.60
3G_5	0.00	0.00	0.01	0.04	0.10	0.22	0.40	0.67	1.03	1.48

charge-symmetry-breaking potentials in the last case. The correlation coefficient of Δa_s and Δa_t turns out to be -0.72 . The values of r_s and r_t are, of course, correlated with the values of a_s and a_t , since the model provides r_s and r_t as functions of a_s and a_t . r_s and r_t become smaller¹⁵ when $|a_s|$ or $|a_t|$ get larger. The statistical errors in a_t are much smaller than in a_s because the Λp cross section is more sensitive to the 3S_1 contribution than to the contribution of the 1S_0 wave because of the statistical factors $\frac{3}{4}$ and $\frac{1}{4}$ for triplet and singlet waves.

When we compare our Λp s -wave scattering lengths and effective ranges which are obtained from the scattering data with the values from the analysis of the s -shell hyperfragments,²⁰ we find almost agreement within the one-standard-deviation bounds for Λp and Λn . We note that our effective ranges in the 1S_0 waves are larger than the ones from the hyperfragment analysis. In a Faddeev-type calculation of the binding energy of ${}^3\Lambda\text{H}$ (Ref. 21) it appeared that larger effective ranges in the 1S_0 waves gave better agreement with the experimental value for the binding energy of the hypertriton. We note that the sign of the theoretical charge-symmetry-breaking potential is the same as in the purely phenomenological treatment in the hyperfragment analysis.²⁰

For the scattering lengths of the charge-symmetric potential (Table V) we just violate in the best-fit point the requirement $|a_s| > |a_t|$, needed because of the spin assignment of ${}^3\Lambda\text{H}$. However, in view of the large statistical error on a_s , this poses no serious problem.

For the six Rehovoth-Heidelberg data we obtain $\chi^2 = 3.1$ and for the six Maryland data $\chi^2 = 1.9$, indicating an excellent fit to the low-energy Λp total cross sections (cf. Table I and Fig. 4). In the momentum region of these data ($p_\Lambda \leq 330$ MeV/c) the total cross sections are strongly dominated by the s waves. Even at $p_\Lambda = 330$ MeV/c the contributions of the higher L waves to the total cross section are still less than 6%. In the calculated angular distributions we have a slight rise in the forward directions and a slight fall in the backward directions in agreement with experiment.¹⁷

TABLE V. Λp , Λn , and Λn scattering lengths and effective ranges in fm. The subscripts s and t refer to the 1S_0 and 3S_1 states, respectively.

	Λp	Λn	Λn
a_s	-1.77 ± 0.28	-1.90 ± 0.30	-2.03 ± 0.32
r_s	3.78 ± 0.35	3.72 ± 0.34	3.66 ± 0.32
a_t	-2.06 ± 0.12	-1.96 ± 0.11	-1.84 ± 0.10
r_t	3.18 ± 0.10	3.24 ± 0.11	3.32 ± 0.11

The Λp elastic total cross sections up to $p_\Lambda = 1$ GeV/c are drawn and compared to experiment in Fig. 4. In the momentum region above 0.3 GeV/c we see a reasonable agreement with the Berkeley data.^{22, 23} In particular we notice that the calculated elastic total cross section in the region 0.6–0.7 GeV/c is well compatible with the experimental point of Berkeley 71 (Ref. 22), but at about two standard derivations away from the point of Berkeley 74 (Ref. 23). We obtain $\chi^2 \approx 14$ for the seven Berkeley 71 data and $\chi^2 \approx 10$ for the seven Berkeley 74 data. The large cusp of 39.0 mb at the $\Sigma^+ n$ threshold is an enhancement in the 3S_1 - 3D_1 waves. This peak is in very good agreement with the results of Ref. 24, where a large peak in the Λp invariant mass is found at $E_{\text{c.m.}} = 2128.7 \pm 0.2$ MeV, the $\Sigma^+ n$ threshold being located at 2128.97 MeV. The large cusp is not due to a multichannel virtual-bound-state resonance, since the eigen phase shift corresponding to the eigenvector, which is dominantly ${}^3S_1(\Lambda p)$, fails to pass through 90° . In fact the maximum value 72.4° of this phase shift is reached just above the $\Sigma^0 p$ threshold. This means that the pole in the 3S_1 - ${}^3D_1(\Sigma N, I = \frac{1}{2})$ amplitudes in the 10^+ , analogous to the deuteron, is not on the second Riemann sheet in the complex energy plane, although it is close to that. Changing the values of the α 's in a large domain does almost not change the position of the pole. When we make the hard-core radius x_t about five standard deviations smaller, a multichannel virtual-bound-state resonance appears at the $\Sigma^0 p$ threshold. However, for this case we have also a Λp bound state. So we conclude that a 3S_1 - ${}^3D_1(\Lambda p)$ virtual-bound-state resonance is unlikely to exist. The situation for Λn is similar.

Before we consider the higher L waves we first mention that we have neglected in the coupled ΛN and ΣN channels the singlet-triplet transitions ${}^1J_J \leftrightarrow {}^3J_J$ ($J \geq 1$). The inclusion of these transitions will not change the results of the fit, since the contributions of the p waves were already small. The contributions of the singlet-triplet transitions are expected to be very small because of the following reasons. In the first place we notice that the antisymmetric spin-orbit potentials, which are responsible for the singlet-triplet transitions, occur only in the scalar-meson and vector-meson potentials [cf. (4.2), (4.3)]. In the scalar-meson case and partially in the vector-meson potential the antisymmetric spin-orbit potential is proportional to mass differences. In exact SU(3) symmetry these contributions will vanish. The only contribution, which survives in exact SU(3) symmetry, appears in the vector-meson potential: the term proportional to $(g_{13}f_{24} - g_{24}f_{13})$ in Eq. (4.3), which means that also here large cancellations

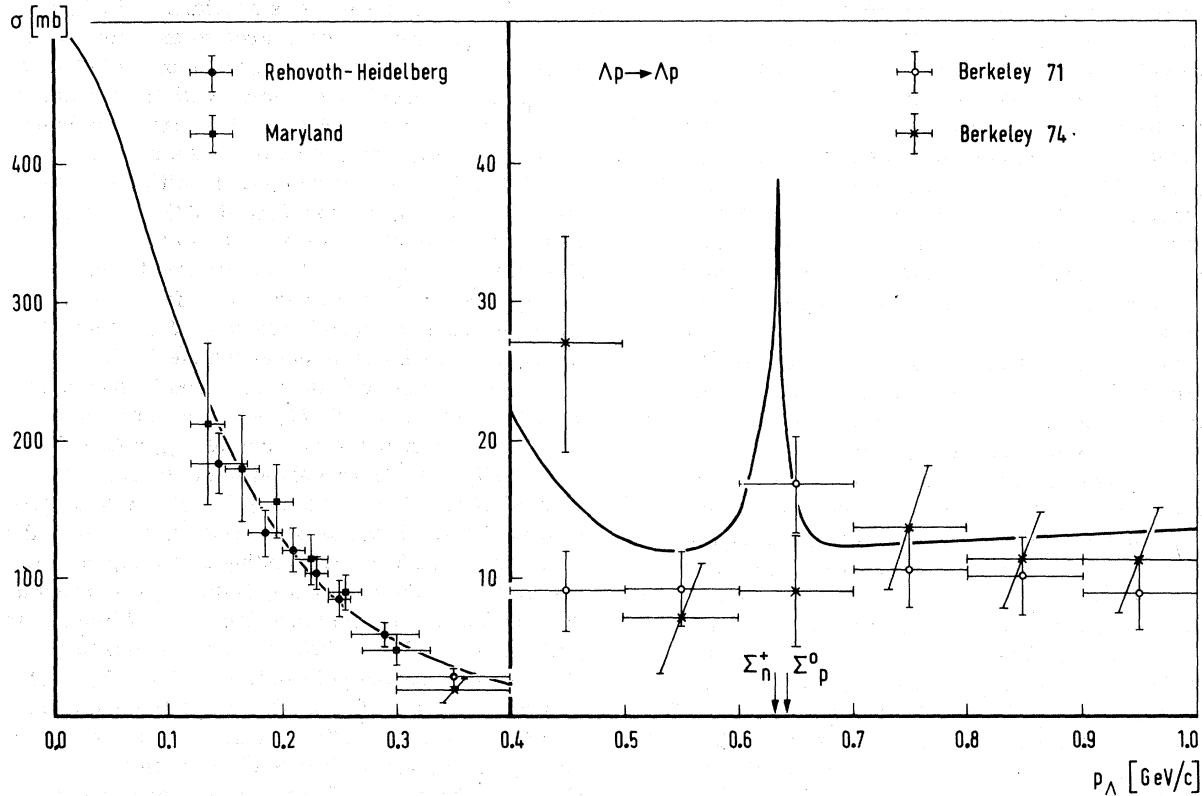


FIG. 4. Calculated Λp elastic total cross sections compared with the Rehovoth-Heidelberg (Ref. 17), Maryland (Ref. 18), and Berkeley data (Refs. 22, 23).

occur. In $\Sigma^+ p$, where the singlet-triplet transitions will vanish in the limit of full SU(3) symmetry, we have seen that the effects of incorporating these potentials are very small. In an energy region where the p and higher waves dominate the scattering the inclusion of singlet-triplet transitions is more important, although the effects are still expected to be small. Neglecting the ${}^3J_J \leftrightarrow {}^1J_J$ transitions has the consequence that we have in general two decoupled 3×3 Schrödinger equations for the 1J_J and 3J_J wave instead of the 6×6 Schrödinger equation for the coupled ${}^1J_J - {}^3J_J$ waves.

The effective-range-expansion parameters for the p waves are given in Table VI for Λp , Λn , and the charge-symmetric state ΛN . The Λp and Λn nuclear-bar phase shifts in the momentum region

TABLE VI. Λp , ΛN , and Λn p -wave effective-range parameters in units of fm.

	Λp		ΛN		Λn	
	a	r	a	r	a	r
1P_1	-0.17	-0.04	-0.20	4.88	-0.22	7.07
3P_0	-0.08	9.76	-0.14	26.0	-0.20	24.6
3P_1	-0.09	57.7	-0.05	64.0	-0.010	-1470
3P_2	-0.26	5.37	-0.26	5.26	-0.26	5.19

below the ΣN thresholds are given in the Tables VII and VIII. We notice that the potentials are overall attractive in all partial waves. The total cross sections for $\Lambda p \rightarrow \Lambda p$, $\Sigma^+ n$, $\Sigma^0 p$ above the ΣN thresholds are given in Table IX. In the region up to roughly $p_\Lambda = 800$ MeV/c there is considerable breaking of the isospin relations between the $\Lambda p \rightarrow \Sigma^+ n$ and $\Lambda p \rightarrow \Sigma^0 p$ cross sections, mainly due to phase-space effects. In Fig. 5 we compare the calculated total cross sections for the experimentally poorly constrained reaction $\Lambda p \rightarrow \Sigma^0 p$ with the data of the Berkeley groups.^{22, 23} The calculated cross sections seem a little lower than the experimental ones, especially with respect to the Berkeley 71 data, yielding $\chi^2 = 5.4$ for four data points. However, a comparison of the total-cross-section data of $\Lambda p \rightarrow \Sigma^0 p$ with $\Sigma^- p \rightarrow \Lambda n$ using isospin relations and detailed balance²⁵ shows a clear discrepancy, indicating that the $\Lambda p \rightarrow \Sigma^0 p$ experimental total cross sections of Ref. 22 are perhaps too high (see also Sec. VD).

D. $\Sigma^- p$ scattering

(i) $\Sigma^- p \rightarrow \Sigma^- p$. The fit to the most recent "total"⁵ cross sections of the Heidelberg groups¹⁹ is given

TABLE VII. Λp nuclear-bar phase shifts below the ΣN thresholds. The phase shifts of the not-displayed $L=4$ waves are smaller than 0.20° everywhere and for $L=5$ smaller than 0.03° .

p_Λ (MeV/c)	100	200	300	400	500	600	633.8
T_{lab} (MeV)	4.5	17.8	39.6	69.5	106.9	151.1	167.5
1S_0	19.07	24.31	21.15	14.66	7.04	-0.64	-2.76
3S_1	21.97	28.48	26.54	21.70	16.57	15.35	38.15
ϵ_1	0.17	0.86	1.96	3.41	5.46	10.35	25.86
3P_0	0.06	0.37	0.67	0.24	-1.39	-4.14	-5.23
1P_1	0.12	0.92	2.76	5.55	9.03	13.37	15.38
3P_1	0.06	0.32	0.63	0.71	0.45	0.35	0.91
3P_2	0.18	1.27	3.50	6.27	8.72	10.30	10.63
ϵ_2	0.00	-0.00	-0.04	-0.13	-0.24	-0.25	-0.17
3D_1	0.00	0.03	0.21	0.71	1.88	5.30	13.66
1D_2	0.00	0.05	0.33	1.08	2.39	4.16	4.81
3D_2	0.00	0.08	0.41	1.19	2.44	3.98	4.53
3D_3	0.00	0.05	0.28	0.86	1.85	3.13	3.58
ϵ_3	0.00	0.00	0.02	0.05	0.13	0.25	0.31
3F_2	0.00	0.00	0.01	0.06	0.21	0.52	0.75
1F_3	-0.00	-0.00	0.00	0.03	0.10	0.24	0.30
3F_3	0.00	0.00	0.02	0.06	0.16	0.30	0.37
3F_4	0.00	0.00	0.02	0.08	0.25	0.56	0.71
σ_{tot} (mb)	309.6	126.7	50.7	22.3	13.1	14.4	39.0

in Table I and Fig. 6. The data are described well and the energy dependence seems good. In Fig. 7 we compare the calculated angular distribution with the experimental one measured by the Heidelberg group.¹⁹ A good description is reached. The shape is essentially determined, apart from the Coulomb forward peak, by the 3S_1 - 3P_1 interference and constructive Coulomb interference.

In Table X we give the total nuclear cross sections for $\Sigma^- p$ elastic scattering up to $p_\Sigma^- = 600$ MeV/c.

The scattering is strongly dominated by the 3S_1 wave for $p_\Sigma^- \leq 300$ MeV/c. At the higher energies the p waves dominate the nuclear total cross sections. The contributions of the higher L waves are always very small.

(ii) $\Sigma^- p \rightarrow \Sigma^0 n$. The calculated total cross sections are compared with the measured values of the Heidelberg group²⁶ in Table I and Fig. 8, showing good agreement. Only the datum at $p_\Sigma^- = 110$ MeV/c is two standard deviations off.

TABLE VIII. Λn nuclear-bar phase shifts in degrees below the ΣN thresholds.

p_Λ (MeV/c)	100	200	300	400	500	600	641.7
T_{lab} (MeV)	4.5	17.8	39.6	69.5	106.9	151.1	171.4
1S_0	21.31	26.46	22.90	16.10	8.26	0.36	-2.51
3S_1	20.04	26.45	24.72	19.98	14.74	11.90	21.09
ϵ_1	0.12	0.70	1.73	3.13	5.03	8.86	17.68
3P_0	0.13	0.68	1.22	0.90	-0.72	-3.56	-4.99
1P_1	0.15	1.07	3.10	6.12	9.84	14.32	16.76
3P_1	0.01	0.08	0.18	0.06	-0.37	-0.77	-0.43
3P_2	0.18	1.26	3.48	6.21	8.59	10.08	10.43
ϵ_2	-0.00	-0.03	-0.11	-0.24	-0.39	-0.43	-0.36
3D_1	0.00	0.05	0.27	0.82	1.96	4.77	10.92
1D_2	0.00	0.07	0.39	1.17	2.53	4.36	5.20
3D_2	0.00	0.05	0.31	1.01	2.17	3.62	4.26
3D_3	0.00	0.05	0.29	0.88	1.87	3.15	3.71
ϵ_3	-0.00	-0.00	-0.00	0.01	0.06	0.17	0.23
3F_2	0.00	0.00	0.02	0.09	0.25	0.56	0.81
1F_3	0.00	0.00	0.02	0.05	0.14	0.30	0.38
3F_3	-0.00	-0.00	-0.00	0.01	0.06	0.17	0.24
3F_4	0.00	0.00	0.02	0.09	0.26	0.58	0.76
σ_{tot} (mb)	284.2	117.9	47.1	20.6	12.1	12.3	23.1

TABLE IX. $\Lambda p \rightarrow \Lambda p$, $\Sigma^+ n$, $\Sigma^0 p$ total cross sections in mb above the ΣN thresholds.

p_Λ (MeV/c)	650	700	750	800	850	900	950	1000
T_{lab} (MeV)	175.5	201.4	228.7	257.2	286.9	317.8	349.7	382.6
$\Lambda p \rightarrow \Lambda p$	15.88	12.41	12.59	12.85	13.09	13.37	13.68	14.05
$\Lambda p \rightarrow \Sigma^+ n$	8.53	8.89	9.79	10.01	9.78	9.30	8.75	8.21
$\Lambda p \rightarrow \Sigma^0 p$	3.02	4.03	4.69	4.92	4.85	4.64	4.36	4.10

The angular distribution has not been measured, because the reaction $\Sigma^- p \rightarrow \Sigma^0 n$ cannot be constrained experimentally. The calculated angular distribution at $p_{\Sigma^-} = 160$ MeV/c looks very much like the one of the reaction $\Sigma^- p \rightarrow \Lambda n$, but systematically about 5 mb lower. The forward-backward asymmetry is mainly caused by the interference of the 3S_1 - 3P_1 and 1S_0 - 1P_1 waves.

In Fig. 9 we compare the calculated total cross sections in the momentum region $150 \leq p_{\Sigma^-} \leq 600$ MeV/c with the unpublished data of the Massachusetts group,²⁷ yielding $\chi^2 = 108$ for nine data points. In the region 350–550 MeV/c the theoretical curve exceeds by several standard deviations the experimental values.

In Table X we give the total cross sections for $\Sigma^- p \rightarrow \Sigma^0 n$ up to $p_{\Sigma^-} = 600$ MeV/c. The scattering is strongly dominated by the 3S_1 wave for $p_{\Sigma^-} \leq 250$ MeV/c. At the higher momenta the p waves dominate the total cross sections. The contributions of the higher L waves are always very small.

(iii) $\Sigma^- p \rightarrow \Lambda n$. In Table I and Fig. 10 we compare the calculated total cross sections with the measured values of the Heidelberg group. The energy dependence seems good.

In Fig. 11 we compare the calculated angular

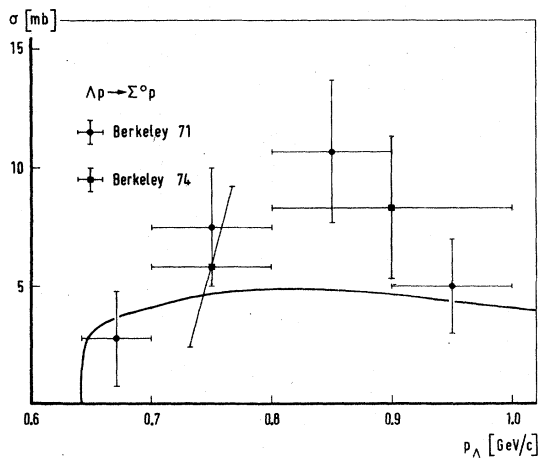


FIG. 5. Calculated $\Lambda p \rightarrow \Sigma^0 p$ total cross sections compared with the data of Refs. 22, 23.

distribution with the experimental data of the Heidelberg group.²⁶ The agreement is good, which is also expressed in the forward-backward ratio, at $p_{\Sigma^-} = 160$ MeV/c, $F/B = 1.51$ compared to the measured value $F/B = 1.40 \pm 0.24$. For the polarization of the outgoing Λ the Heidelberg group²⁶ has measured, in the region 100–170 MeV/c $\langle \vec{P} \cdot \hat{n} \rangle = -0.6 \pm 0.4$. Since most of the events are in the higher-momentum region we compare it with the calculated value at $p_{\Sigma^-} = 150$ MeV/c $\langle \vec{P} \cdot \hat{n} \rangle = -0.25$.

In Fig. 12 we compare the calculated total cross sections in the momentum region $150 \leq p_{\Sigma^-} \leq 600$ MeV/c with the unpublished data of the Massachusetts group,²⁷ yielding $\chi^2 = 75$ for nine data. The theoretical cross sections are larger at most energies than the Massachusetts data. However, we mentioned already in the discussion of $\Lambda p \rightarrow \Sigma^0 p$ a discrepancy between those data and the ones for $\Sigma^- p \rightarrow \Lambda n$ when using isospin relations and detailed

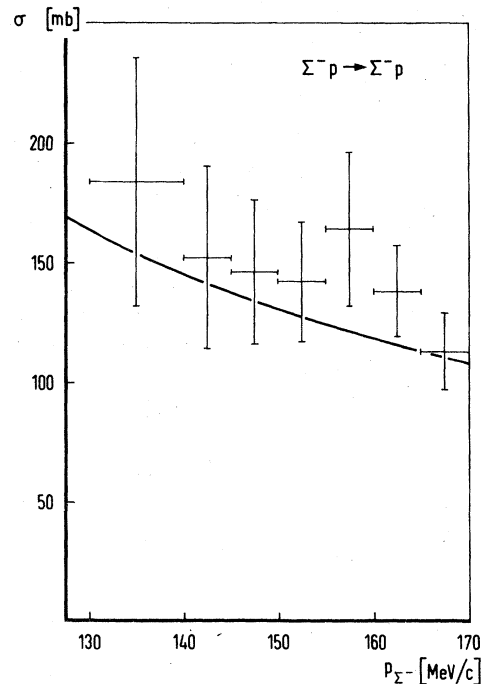


FIG. 6. Calculated $\Sigma^- p$ elastic "total" cross sections compared with the experimental data (Ref. 19).

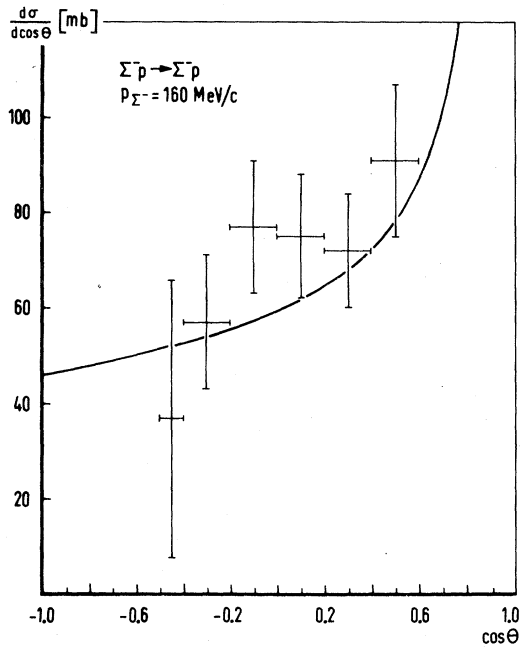


FIG. 7. Calculated Σ^-p elastic differential cross section compared with the data (Ref. 19).

balance. The dashed points in Fig. 12 have been calculated this way. So our calculations suggest with respect to the aforementioned discrepancy that the $\Sigma^-p \rightarrow \Lambda n$ data of the Massachusetts group are too small, whereas the Berkeley data on $\Lambda p \rightarrow \Sigma^0 p$ are a little high.

In Table X we give the total cross sections for $\Sigma^-p \rightarrow \Lambda n$ up to $p_{\Sigma^-} = 600$ MeV/c. The scattering is strongly dominated by the ${}^3S_1 \rightarrow {}^3S_1$ and ${}^3S_1 \rightarrow {}^3D_1$ transitions for $p_{\Sigma^-} \leq 250$ MeV/c. At higher momenta the p waves dominate the total cross sections. The contributions of the higher L waves are always very small.

Since it has become feasible to do Σ^-p scattering with a polarized beam, we present for the reaction $\Sigma^-p \rightarrow \Lambda n$ the calculated values for the measurable quantities (averages or differential cross sections and averaged polarizations), because the Λ is an excellent polarization analyzer. Thereby we have included the amplitudes of the s and p waves and of the ${}^3S_1 \rightarrow {}^3D_1$ and ${}^3P_2 \rightarrow {}^3F_2$ transitions.

TABLE X. $\Sigma^-p \rightarrow \Sigma^-p$, $\Sigma^0 n$, Λn total nuclear cross sections in mb.

p_{Σ^-} (MeV/c)	50	100	150	200	250	300	350	400	450	500	550	600
T_{lab} (MeV)	1.0	4.2	9.4	16.6	25.8	37.0	50.1	65.0	81.8	100.2	120.3	141.9
$\Sigma^-p \rightarrow \Sigma^-p$	518.7	214.4	122.5	82.0	63.8	57.0	55.3	54.4	52.9	50.7	48.2	45.5
$\Sigma^-p \rightarrow \Sigma^0 p$	696.8	224.3	120.7	83.3	67.5	59.9	54.3	48.2	42.0	36.4	31.8	28.0
$\Sigma^-p \rightarrow \Lambda n$	984.4	281.4	134.8	83.6	60.8	48.7	40.9	35.2	30.5	26.6	23.3	20.5

When we want to compare our predictions (Table XI) with the measurements of the Massachusetts group we are hampered by the small statistics in the experiment. The value for the forward-backward asymmetry $(F - B)/(F + B)$ in the momentum range with by far the largest number of events $50 \leq p_{\Sigma^-} \leq 100$ MeV/c agrees with our result. We estimate from the experiment in this band $(F - B)/(F + B) = 0.06 \pm 0.06$. When we multiply our values for the averaged left-right asymmetry $\bar{\epsilon}$ with the experimental initial Σ^- polarizations P_1^i , we get values for the left-right asymmetry in the angular distributions $(L - R)/(L + R) = P_1^i \bar{\epsilon}$ close to 0. In the band 50–100 MeV/c our values for $\bar{\epsilon}$ together with the experimental value for P_1^i leads to $(L - R)/(L + R) = -0.015 \pm 0.011$, whereas the experimental result reads -0.05 ± 0.06 . For the polarization along the normal,²⁷ in the momentum region with the best statistics 50–100 MeV/c, the Massachusetts group found $(\bar{P} \cdot \hat{n}) = -0.11 \pm 0.10$ in agreement with our values (Table XI). The experimental situation concerning the average depolarization \bar{D} makes any comparison at all senseless. The average asymmetries of the component of the final polarization in the direction perpendicular to the normal and the incident momentum, \bar{Q}^\perp (such that a right-handed coordinate system is formed by the three directions), and of the component of the final polarization along the incident momentum, \bar{Q}^\parallel , both with respect to the plane perpendicular to the initial polarization have not been measured. This is unfortunate since these are predicted to have reasonably large values (Table XI).

Finally, we want to mention for the inelastic-capture ratio at rest that we have obtained $r_R = 0.4775$ in good agreement with the averaged experimental value⁴ $r_R = 0.468 \pm 0.010$.

VI. DISCUSSION

A. Coupling constants

The values of the NN coupling constants have been discussed in paper I. Here we shall be concerned with the meson-baryon couplings involving nonzero strangeness. These are calculated via SU(3) with the inputs (i) the octet coupling g_8 , (ii) the $\alpha = F/(F + D)$ ratio, (iii) the singlet-octet mix-

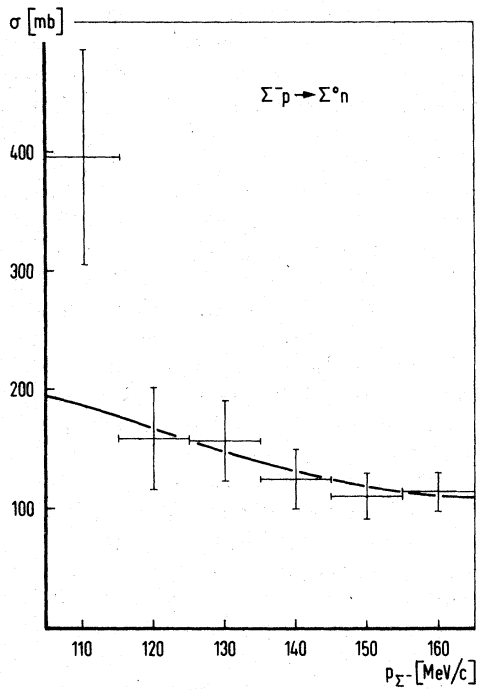


FIG. 8. Calculated $\Sigma^- p \rightarrow \Sigma^0 n$ total cross sections compared with the experimental values (Ref. 26).

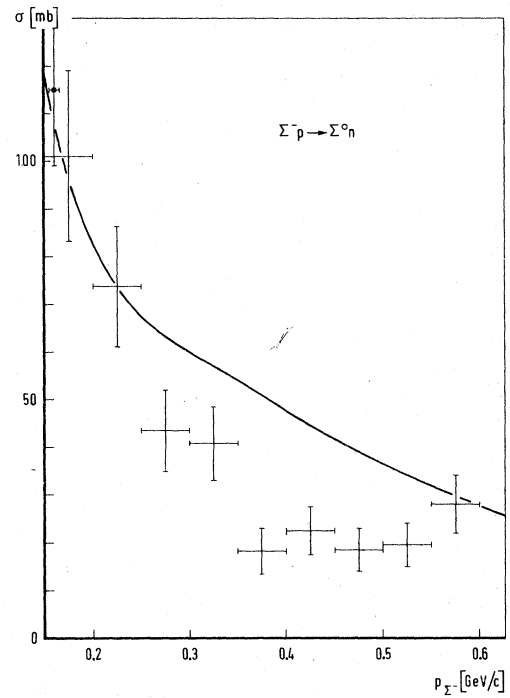


FIG. 9. Calculated $\Sigma^- p \rightarrow \Sigma^0 n$ total cross sections compared with the data of the Massachusetts group (Ref. 27). The datum with the black square is from the Heidelberg group (Ref. 26).

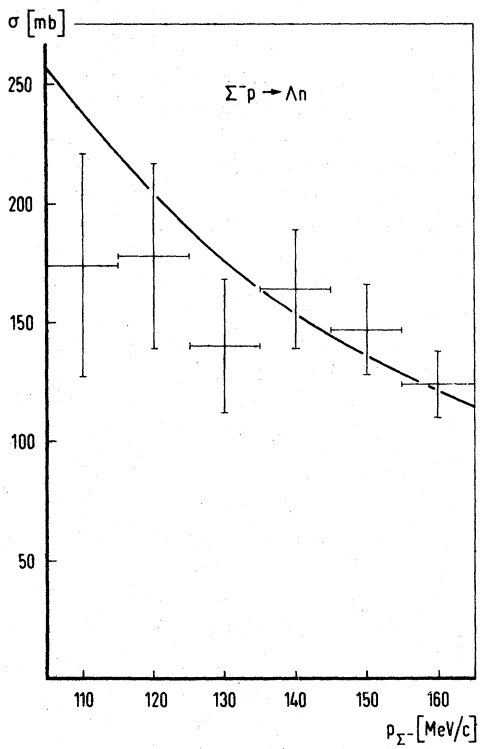


FIG. 10. Calculated $\Sigma^- p \rightarrow \Lambda n$ total cross sections compared with the experimental values (Ref. 26).

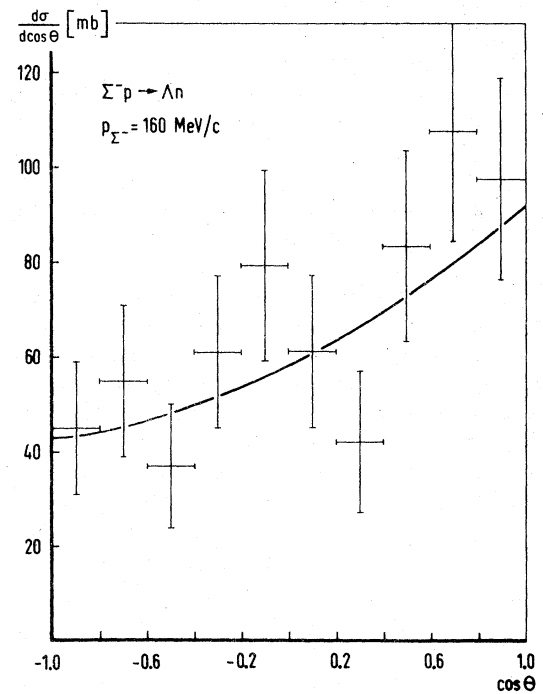


FIG. 11. Calculated differential cross section for the reaction $\Sigma^- p \rightarrow \Lambda n$ compared with the experimental angular distribution (Ref. 26).

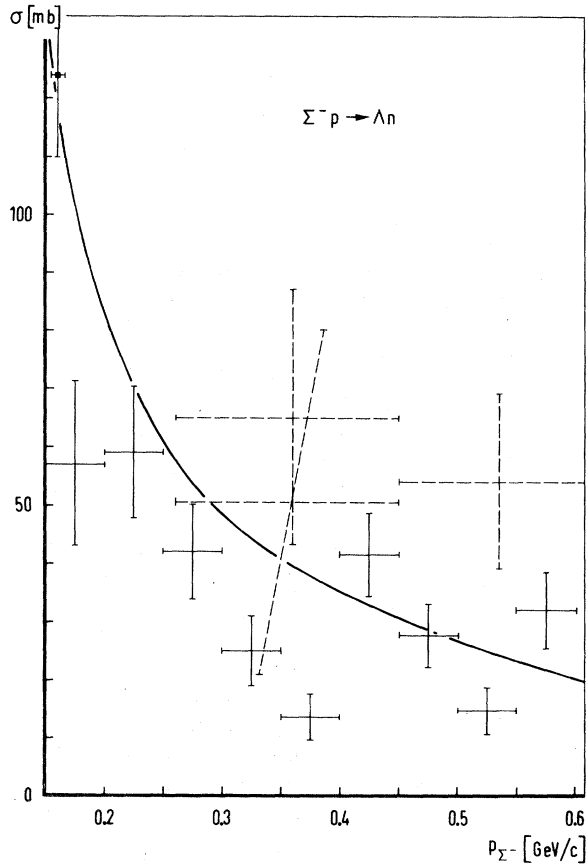


FIG. 12. Calculated $\Sigma^- p \rightarrow \Lambda n$ total cross sections compared with the data of the Massachusetts group (Ref. 27). The datum with the black square is from the Heidelberg group (Ref. 26). The dashed data have been calculated from the results for $\Lambda p \rightarrow \Sigma^0 p$ (Refs. 22, 23) using isospin relations and detailed balance.

ing angle θ , (iv) the singlet coupling constant g_1 . The values for these parameters are given in Table XII. Inserting these values in the SU(3) relations and the mixing relations for the coupling constants leads to the couplings of Table XIII.

The discussion of the coupling constants involving nonzero strangeness will deal practically only with the pseudoscalar mesons, since there is virtually no information from other sources about the coupling constants of the vector mesons to strange baryons. In the first place we mention that our value (assuming pseudoscalar coupling) $\alpha_p = 0.464 \pm 0.012$ is not too far from the SU(6) value $\alpha_p = 0.4$. Most determinations in the literature² are based on the comparison of some pseudoscalar-meson coupling constant at a vertex involving strange baryons with the πN coupling. Often a result around $\alpha_p = 0.4$ is reached. But it is hard to come to a more definite conclusion because of the problems concerning $g_{\Lambda\Sigma\pi}$ and $g_{\Lambda NK}$ (see below). One of the advantages

TABLE XI. Calculated measurable quantities for $\Sigma^- p \rightarrow \Lambda n$ at various lab momenta in MeV/c.

P_{Σ^-}	$\frac{F-B}{F+B}$	$\frac{P-E}{P+E}$	$\bar{\epsilon}$	$\langle \vec{P} \cdot \hat{n} \rangle$	\bar{D}	$\bar{\alpha}^+$	$\bar{\alpha}^0$
50	0.03	0.00	0.02	-0.08	0.27	0.13	-0.03
100	0.09	0.01	0.04	-0.18	0.24	0.08	-0.10
150	0.18	0.03	0.06	-0.25	0.18	-0.01	-0.21
200	0.29	0.06	0.08	-0.26	0.09	-0.14	-0.34
250	0.37	0.10	0.09	-0.20	0.00	-0.27	-0.45
300	0.42	0.14	0.09	-0.12	-0.07	-0.39	-0.52
350	0.43	0.19	0.09	-0.05	-0.13	-0.49	-0.56
400	0.41	0.24	0.07	0.00	-0.17	-0.57	-0.58
450	0.38	0.28	0.06	0.03	-0.19	-0.61	-0.57
500	0.34	0.32	0.04	0.05	-0.21	-0.64	-0.55
550	0.30	0.35	0.03	0.06	-0.22	-0.66	-0.54
600	0.26	0.37	0.02	0.06	-0.23	-0.66	-0.52

we have in the determination of α_p is that α_p enters in a simultaneous NN and YN analysis in many coupling constants ($NN\eta_8$, $\Sigma\Sigma\pi$, ΛNK , ΣNK , $\Lambda\Lambda\eta_8$, $\Sigma\Sigma\eta_8$) in contrast to other analyses, where usually one or two of the aforementioned couplings are met. This leads perhaps to a more direct determination of α_p .

We start comparing our resulting coupling constants with the values from the literature with the least controversial ones, $g_{\Sigma\Sigma\pi}$ and $g_{\Lambda\Sigma\pi}$. Values of about $g_{\Sigma\Sigma\pi}^2/4\pi \approx 13 \pm 2$ are given in the compilation of coupling constants,² and they agree well with our value $g_{\Sigma\Sigma\pi}^2/4\pi = 11.5$. Values of $g_{\Lambda\Sigma\pi}^2 \approx 11 \pm 1$ are obtained² for the $\Lambda\Sigma\pi$ coupling, which are considerably larger than our value $g_{\Lambda\Sigma\pi}^2 = 5.1$. The large values in the literature for both $g_{\Sigma\Sigma\pi}$ and $g_{\Lambda\Sigma\pi}$ are sometimes considered as evidence for the pseudovector coupling to obey SU(3) symmetry.²⁸ However, this leads to a rather large value of $g_{\Lambda NK}^2/4\pi$, which seems to contradict in turn the determinations of this coupling constant. From $K^\pm N$ forward dispersion relations it is clear that $g_{\Sigma NK}^2/4\pi$ is very small (≤ 1).² For the ΛNK coupling the results can be grouped into two bands, $4 \lesssim g_{\Lambda NK}^2/4\pi \lesssim 7$ and $8 \lesssim g_{\Lambda NK}^2/4\pi \lesssim 14$, with statistical errors of about 2.² It seems to us that the latter estimates are more reliable than the former ones because of the theoretically better

TABLE XII. Parameters to be used in the SU(3) relations for the pseudoscalar (P), direct vector (V_8), derivative vector (V_m), and scalar (S) meson coupling constants.

	$g_8/\sqrt{4\pi}$	α	θ	$g_1/\sqrt{4\pi}$
P	3.660 00	0.464 03	-10.4°	4.316 75
V_8	0.594 44	1	35.264 30°	3.403 12
V_m	4.816 96	0.334 28	35.264 30°	2.202 86
S	5.032 08

TABLE XIII. Coupling constants at vertices involving strange baryons.

	$\Sigma\Sigma\pi$	$\Lambda\Sigma\pi$	ΛNK	ΣNK	$\Lambda\Lambda\eta$	$\Sigma\Sigma\eta$	$\Lambda\Lambda X^0$	$\Sigma\Sigma X^0$
$g/\sqrt{4\pi}$	3.40	2.27	-4.07	0.26	-1.45	2.56	4.65	3.84
	$\Sigma\Sigma\rho$	$\Lambda\Sigma\rho$	ΛNK^*	ΣNK^*	$\Lambda\Lambda\phi$	$\Sigma\Sigma\phi$	$\Lambda\Lambda\omega$	$\Sigma\Sigma\omega$
$g/\sqrt{4\pi}$	1.19	0	-1.03	-0.59	-1.96	-1.96	2.78	2.78
$f/\sqrt{4\pi}$	3.22	3.70	-4.64	1.60	-4.30	1.75	-0.34	3.94

parametrization of the unphysical region; an effective-range parametrization for $\bar{K}N$ in contrast to a zero-range approximation or constant scattering length parametrization for $\bar{K}N$. More recent analyses using many different inputs or constraints for the unphysical region show for the coupling $g_Y^2 = (g_{\Lambda NK}^2 + 0.84 g_{\Sigma NK}^2)/4\pi$ also typically results in two bands, $g_Y^2 \approx 14 \pm 4$ or $g_Y^2 \approx 8 \pm 2$.² Perhaps the values for $(g_{\Lambda NK}^2 + g_{\Sigma NK}^2)/4\pi = 15.2 \pm 2.3$ (Ref. 29) or $g_Y^2 = 15.2 \pm 0.7$ (Ref. 30) from K^+p phase-shift analyses are less model dependent. These values are compatible with ours, $(g_{\Lambda NK}^2 + g_{\Sigma NK}^2)/4\pi = 16.7$. The conclusion we would like to draw from this comparison is that probably our value for α_p is a little high. A somewhat smaller value would raise $g_{\Lambda\Sigma\pi}$ and lower $g_{\Lambda NK}$ and $g_{\Sigma\Sigma\pi}$ leading to a better general agreement with the values of the literature. Perhaps the determinations of the K couplings are systematically too low, such that one should prefer pseudovector coupling above pseudoscalar coupling in view of the large values for both $g_{\Lambda\Sigma\pi}$ and $g_{\Sigma\Sigma\pi}$ in the literature.

Finally, we mention that the value from the YN fit $\alpha_V^m = 0.334 \pm 0.002$ is not too far from the prediction of $SU(6)$, $\alpha_V^m = 0.4$ (see, e.g., the reviews Refs. 31 and 32).

B. Results

Although the obtained $\chi^2/\text{data} = 0.65$ is low, it does not imply that it is trivial to obtain good fits simultaneously to $\Lambda p \rightarrow \Lambda p$, $\Sigma^+ p \rightarrow \Sigma^+ p$, $\Sigma^- p \rightarrow \Sigma^- p$, $\Sigma^- p \rightarrow \Sigma^0 n$, and $\Sigma^- p \rightarrow \Lambda n$ in spite of the rather large statistical errors. The constraints between Λp and $\Sigma^- p$ scattering are strong in our model, especially in the coupled 3S_1 - 3D_1 waves. One of the important features in the equality of the $\Lambda\Lambda\epsilon$ and $\Sigma\Sigma\epsilon$ coupling due to the assumption of the ϵ meson being a unitary singlet. This can be illustrated best when contributions of an octet of scalar mesons are also considered, as well as singlet-octet mixing. Then it appears⁶ that only when the $\Lambda\Lambda\epsilon$ and $\Sigma\Sigma\epsilon$ couplings are nearly equal a simultaneous fit to Λp and $\Sigma^- p$ scattering is possible. When this is not the case, it is not possible by changing the free parameters to bring

both the Λp and $\Sigma^- p$ cross sections in accordance with the experimental values.

The good fit to the $\Sigma^+ p$ "total" cross sections is mainly caused by two facts: The 3S_1 contribution is always small, and we have essentially a free parameter for the 1S_0 wave. It appears that the 1P_1 phase shift resonates almost at higher energies. In fact, when we make the hard-core radius a little smaller, the fit to the low-energy differential cross sections remains almost as good as before, allowing at the same time as 1P_1 resonance.

For Λp scattering we obtain a better fit to the low-energy data than in model A,⁵ since the s -wave effective ranges are considerably larger in this model D. It is unlikely in our model that there is a resonance in the 3S_1 - 3D_1 waves in the neighborhood of the ΣN thresholds, although a large cusp appears at the $\Sigma^+ n$ threshold in the elastic Λp channel. Above the ΣN thresholds the calculated $\Lambda p \rightarrow \Lambda p$ total cross sections agree reasonably and the $\Lambda p \rightarrow \Sigma^0 p$ total cross sections are a little lower than the Berkeley data.

For $\Sigma^- p$ scattering into $\Sigma^- p$, $\Sigma^0 n$, and Λn we have good fits for the low-energy data on total cross sections, angular distributions, and the branching ratio at rest. The branching of $\Sigma^- p$, into $\Sigma^- p$, $\Sigma^0 n$, and Λn largely determined the value of the $F/(F+D)$ ratio for the assumed pseudoscalar coupling for the pseudoscalar-meson octet. At the higher energies the calculated values for the total cross sections in the reaction $\Sigma^- p \rightarrow \Sigma^0 n$ come out considerably larger than the measured values of the Massachusetts group, especially in the region where the p waves dominate the total cross sections. Also the calculated total cross sections for $\Sigma^- p \rightarrow \Lambda n$ at higher energies seem higher than the Massachusetts data.

ACKNOWLEDGMENT

Part of this work was included in the research program of the Stichting voor Fundamenteel Onderzoek der Materie (F.O.M.) with financial support from the Nederlandse Organisatie voor Zuiver-Wetenschappelijk Onderzoek (Z.W.O.).

*Present address: Michigan State University, East Lansing, MI, USA.

¹M. M. Nagels, T. A. Rijken, and J. J. de Swart, Phys. Rev. D **12**, 744 (1975).

²H. Pilkuhn, W. Schmidt, A. D. Martin, C. Michael, F. Steiner, B. R. Martin, M. M. Nagels, and J. J. de Swart, Nucl. Phys. **B65**, 460 (1973).

³*Proceedings of the International Conference on Hypernuclear Physics, Argonne National Laboratory, 1969*, edited by A. R. Bodmer and L. G. Hyman (Argonne National Laboratory, Argonne, Illinois, 1969).

⁴J. J. de Swart, M. M. Nagels, T. A. Rijken, and P. A. Verhoeven, *Springer Tracts in Modern Physics*, edited by G. Höhler (Springer, New York, 1971), Vol. 60, p. 138.

⁵M. M. Nagels, T. A. Rijken, and J. J. de Swart, Ann. Phys. (N.Y.) **79**, 338 (1973).

⁶M. M. Nagels, T. A. Rijken, and J. J. de Swart, in *Few Particle Problems in the Nuclear Interaction*, edited by I. Slaus, S. A. Moszkowski, R. P. Haddock, and W. T. H. van Oers (North-Holland, Amsterdam, 1972), p. 42.

⁷M. M. Nagels, T. A. Rijken, and J. J. de Swart, Phys. Rev. Lett. **31**, 569 (1973).

⁸Our conventions are

$$p^\mu = (E(\vec{p}), \vec{p}), \quad p^2 = p^\mu p_\mu = -M^2,$$

$$\gamma^0 = i\rho_3, \quad \vec{\gamma} = \rho_2 \vec{\sigma}, \quad \gamma_5 = -\rho_1, \quad \sigma_{\mu\nu} = [\gamma_\mu, \gamma_\nu]/2i.$$

Dirac equation:

$$(i\gamma \cdot p + M)u(\vec{p}, s) = 0 = \bar{u}(p, s) (i\gamma \cdot p + M),$$

$$(i\gamma \cdot p - M)v(\vec{p}, s) = 0 = \bar{v}(p, s) (i\gamma \cdot p - M),$$

$$u(\vec{p}, s) = (E+M)^{-1/2} \begin{pmatrix} (E+M)\chi_s \\ \vec{\sigma} \cdot \vec{p} \chi_s \end{pmatrix}.$$

⁹A. A. Logunov and A. N. Tavkhelidze, Nuovo Cimento **29**, 380 (1963).

¹⁰R. Blankenbecler and R. Sugar, Phys. Rev. **142**, 1051 (1966).

¹¹A. Gersten, P. A. Verhoeven, and J. J. de Swart, Nuovo Cimento **26A**, 375 (1975).

¹²M. H. Partovi and E. L. Lomon, Phys. Rev. D **2**, 1999 (1970).

¹³J. M. Charap and S. P. Fubini, Nuovo Cimento **14**, 540 (1959); **15**, 73 (1960).

¹⁴S. Okubo and R. E. Marshak, Ann. Phys. (N.Y.) **4**, 166 (1958).

¹⁵M. M. Nagels, Ph.D. thesis, Univ. of Nijmegen, Nijmegen, The Netherlands, 1975 (unpublished).

¹⁶N. Hoshizaki and S. Machida, Prog. Theor. Phys. **24**, 1325 (1960).

¹⁷G. Alexander, U. Karshon, A. Shapira, G. Yekutieli, R. Engelmann, H. Filthuth, and W. Lughofer, Phys. Rev. **173**, 1452 (1968).

¹⁸B. Sechi-Zorn, B. Kehoe, J. Twitty, and R. A. Burnstein, Phys. Rev. **175**, 1735 (1968).

¹⁹F. Eisele, H. Filthuth, W. Föhlisch, V. Hepp, E. Leitner, and G. Zech, Nucl. Phys. **B37**, 204 (1971).

²⁰R. H. Dalitz, R. C. Herndon, and Y. C. Tang, Nucl. Phys. **B47**, 109 (1972).

²¹B. F. Gibson and D. R. Lehmann, Phys. Rev. C **10**, 888 (1974).

²²J. A. Kadyk, G. Alexander, J. H. Chan, P. Gaposchkin, and G. H. Trilling, Nucl. Phys. **B27**, 13 (1971).

²³J. M. Hauptman, LBL Report No. LBL-3608, 1974 (unpublished).

²⁴T. H. Tan, Phys. Rev. Lett. **23**, 395 (1969).

²⁵G. Alexander and O. Benary, in *Proceedings of the Amsterdam International Conference on Elementary Particles, 1971*, edited by A. G. Tenner and M. J. G. Veltman (North-Holland, Amsterdam, 1971), p. 417.

²⁶R. Engelmann, H. Filthuth, V. Hepp, and E. Kluge, Phys. Lett. **21**, 587 (1966).

²⁷D. Stephen, Ph.D. thesis, Univ. of Massachusetts, 1970 (unpublished).

²⁸H. Pilkuhn, *Springer Tracts in Modern Physics*, edited by G. Höhler (Springer, New York, 1970), Vol. 55, p. 168.

²⁹R. C. Miller, T. B. Novey, A. Yokosawa, R. E. Cutkosky, H. R. Hicks, R. L. Kelly, C. C. Shih, and G. Burleson, Nucl. Phys. **B37**, 401 (1972).

³⁰W. N. Cottingham, A. C. Davis, D. I. Giddings, Nucl. Phys. **B91**, 509 (1975).

³¹B. Sakita, in *Advances in Particle Physics*, edited by R. L. Cool and R. E. Marshak (Interscience, New York, 1968), Vol. 1, p. 219.

³²A. Pais, Rev. Mod. Phys. **38**, 215 (1966).